Formation and evolution of glauconite in the Demerara Contourite depositional system related to NADW circulation changes during late Quaternary (French Guiana)

Cédric Tallobre, Pierre Giresse, Maria-Angela Bassetti, Lies Loncke, Germain Bayon, Roselyne Buscail, Alina Tudryn, Sébastien Zaragosi

Formation and evolution of glauconite in the Demerara Contourite Depositional system related to NADW circulation changes during late Quaternary (French Guiana)

Cédric Tallobre[1,2,3], Pierre Giresse[1,3], Maria-Angela Bassetti[1,3], Lies Loncke[1,3], Germain Bayon[4], Roselyne Buscail[3,1], Alina Tudryn[5] , Sébastien Zaragosi[6]

Corresponding author: cedric.tallobre@univ-perp.fr

[1] Univ. Perpignan Via Domitia, Centre de Formation et de Recherche sur les Environnements Méditerranéens (CEFREM), UMR 5110, 52 Avenue Paul Alduy, 66860 Perpignan, France.

[2] Univ. Littoral Côte d'Opale, Laboratoire d'Océanologie et de Géosciences (LOG), UMR 8187 LOG, 52 28 Avenue du Maréchal Foch, 62930 Wimereux, France (present adress).

[3] CNRS, Centre de Formation et de Recherche sur les Environnements Méditerranéens (CEFREM), UMR 5110, 52 Avenue Paul Alduy, 66860 Perpignan, France

[4] IFREMER, Unité de Recherche Géosciences Marines, 29280 Plouzané, France.

[5] GEOPS, Univ. Paris-Sud, CNRS, Université Paris-Saclay, Rue du Belvédère, Bât. 504-509, 91405 Orsay, France.

[6] Université de Bordeaux, Environnements et Paléoenvironnements Océaniques et Continentaux, UMR CNRS 5805 EPOC, Allée Geoffroy Saint-Hilaire - CS 50023 - 33615 Pessac cedex - France

A. Abstract

The Demerara Plateau is a marginal plateau which forms a bathymetric relief on the sea floor. Here, contourite deposits have been studied in detail, following the recent discovery of contourite sequences likely related to the bottom currents and linked both to contour current and peculiar sea-floor morphology. A chronostratigraphic framework, based on $\delta^{18}O$ relative variations and palaeomagnetic events in sediment cores allows correlating sediment processes to current intensity changes and major climate phases (glacial or interglacial). The studied sediments are enriched in glauconitic grains. In addition, the glauconite mineralogical maturity can easily correlate to low sedimentation rate and slightly energetic bottom currents on the seafloor. Based on these data and using the glauconitic authigenic mineral as proxy for

inferring the degree of winnowing at the sediment-water interface, we might put forward the hypothesis that the intensity of NADW is higher during the glacial stages and lower during interglacial periods.

Keywords: marginal plateau, contourite, glauconite, Demerara Plateau

B. Introduction

Contourites are sediments deposited or reworked by the action of a persistent bottom current. The identification of sedimentary structures on the seafloor induced by current activity introduces the concept of contourites by Heezen (1959), Heezen and Johnson (1963), and Heezen and Hollister (1964). The presence of contourites is marked by a set of different depositional and erosional structures at different scales. All of these structures and their evolution compose a 'Contourite Depositional System' or CDS (Rebesco and Camerlenghi, 2008).

Contourites are generally characterized by a graded and often bioturbated sedimentary sequence (Faugères et al., 1984; Gonthier et al., 1984; Stow et al., 2002; Stow and Faugères, 2008a; Rebesco et al., 2014; Shanmugam, 2016). The ideal sequence was established by Faugères et al. (1984) and Gonthier et al. (1984) and completed by Stow and Faugères (2008a). The alternation of positive and inverse grading sequences, composed of 5 units from C1 to C5, might record velocity current variations through time. The ideal contourite sequence is composed of the C1 to C5 units:

- Unit C1 is the mud unit rich in clays, in fine silt without lamination and rich in bioturbation structures. This unit corresponds to a low current velocity;
- Unit C2, mottled silt and mud, is coarser than C1 with silty lenses and bioturbation;

- Unit C3 is characterized by coarsening upward sediment grain size that increases Bioturbation might be strong and can destroy laminations. Erosional surfaces are possible, linked to high bottom current activity;
- Unit C4: mottled silt and mud, with silty lenses and bioturbation
- Unit C5: mud unit rich in clays and in fine silt without lamination and rich in bioturbation structures, and this unit correspond to a low current velocity.

C1 to C3 corresponds to the positive graded sequence generated by increasing current intensity and C3 to C5 to the negative (inverse) graded sequence following the decrease of current intensity (Faugères et al., 1984; Gonthier et al., 1984; Stow and Faugères, 2008b). The sedimentation can sometimes be affected by diagenetic processes with the formation of authigenic concretions such as nodules and/or encrustations of manganese, as well glauconitic grains, as reported by several authors (Bahk et al., 2001; Giresse and Wiewióra, 2001; Lee et al., 2004; Bahk et al., 2005; Stow and Faugères, 2008a; Faugères and Mulder, 2011).

According to the existing literature (Banerjee et al., 2016), the formation of glauconitic grains is mainly associated to low sedimentation rate on the continental shelf whereas the glauconitisation process in deep marine environments is poorly known. Some authors relate the low sediment accumulation rates to winnowing effect at the sediment-water interface (Chafetz and Reid, 2000; Giresse and Wiewióra, 2001; Wiewióra et al., 2001; Giresse, 2008). Glaucony is a greenish grain which belongs to the glauconite mineral family, and which forms inside shells (often foraminifer tests) or pellets or biotite sheets (McRae, 1972; Odin, 1988; Giresse and Wiewióra, 2001; Wiewióra et al., 2001; Giresse, 2008; Banerjee et al., 2016).

One of the objectives of the IGUANES oceanographic cruise (2013) on the Demerara Plateau (French Guiana) was to shed lights on the sedimentary processes at the origin of the observed depositional sequences, possibly in relation with climate oscillations. This site has been found to host a CDS, yielding sediments rich in authigenic grains of glaucony. In this work, a major element analysis of the green glauconitic grains has been carried out with the objective of understanding the possible role of bottom current velocity in the early diagenetic processes forming glaucony and, consequently, to use this tool as a proxy for bottom current intensity.

C. Background of the study area

The Atlantic margin of the South American continent is affected by extended contouritic processes in several places, such as along the Argentina or Brazil margins (Viana et al., 1998; Faugères et al., 2002; Hernández-Molina et al., 2009; Rebesco et al., 2014; Shanmugam, 2016). The Demerara plateau, which forms a seafloor salient prolonging the continental shelf down to ~ 3400m depth (Fig.1-2), has been described as a site where bottom currents might have strong control over the shape of the seafloor. The morphology of this plateau is thought to be at the origin of the contourite deposits, since it might favour the acceleration of bottom currents (Loncke et al., 2016; Tallobre et al., 2016).

I. Oceanographic setting

The Demerara Plateau is located at latitude N 7°30 between the Equator and the Tropic of Cancer (Fig.1), climatically under the influence of the InterTropical Convergence Zone (ITCZ), whose northern limit is at N 10° during the boreal summer (Müller-Karger et al., 1989; Arz et al., 1999; López-Otálvaro et al., 2009). The main water masses controlling the hydrodynamism in this area are (Reid, 1989; Peterson and Stramma, 1991; Tsuchiya et al., 1994; Stramma and Schott, 1999):

- The surface water with the Tropical Surface Water (TSW) and the North Tropical Gyre
- The Antarctic Intermediate Water (AAIW) formed in the Southern Ocean

- The deep water masses composed by the North Atlantic Deep Water (NADW) derived from the North Atlantic and Arctic Seas, and the Antarctic Bottom Water (AABW) formed around Antarctica (Fig.1).

II. Geological setting

The Demerara Plateau is a marginal plateau (Loncke et al., 2016; Mercier de Lépinay et al., 2016) located at the junction between the Central and Equatorial Atlantic Oceans (Fig.1). It is the conjugate margin of the Guinean Plateau. These two plateaus were initially separated by a transform fault. The marginal plateau of Demerara forms an indentation, an overhang on the seafloor that is 160 km wide and 350 km long (Fig.1), ranging from water depths of 200 to 3800 m (Fig.2).

This bathymetric relief hosts two main types of sedimentation along its outer edge: mass transport deposit and contourites (Hurley et al., 1967; Ingram, 2006; Loncke et al., 2009; Gaullier et al., 2010; Pattier et al., 2013; Loncke et al., 2016). The main mass transport deposit (MTD) accumulations occurred between the Oligocene and the Pleistocene (Pattier et al., 2013; Pattier et al., 2015). The associated slope failure trace is still imprinted on the present-day bathymetry, forming a linear slope failure headscarp over 150 km in length that parallels the distal transform marginal plateau boundary (Loncke et al., 2016).

The impact of the bottom current on the construction and evolution of the CDS along the Demerara Plateau is highlighted by recent studies (Loncke et al., 2009; Pattier et al., 2015; Loncke et al., 2016; Tallobre et al., 2016). The presence of the marginal plateau, an overhang on the seafloor, enables the intensification of the NADW (NW-SE) and promotes the formation of contourites on the Demerara plateau. Many erosional features, such as NW-SE oriented comet marks, have been identified and attest of the impact of bottom current on the seafloor structures.

III. Climate general features of the study area

The global climate oscillations are known through the study of various marine $\delta^{18}O$ record areas in the Western Equatorial Atlantic (Arz et al., 1998; Lisiecki and Raymo, 2005; López-Otálvaro et al., 2009; Lopes et al., 2014). Past climate changes in this area have driven latitudinal migrations of the position of the ITCZ, generating differences in precipitation rates and atmospheric humidity (Arz et al., 1999; López-Otálvaro et al., 2009; Kageyama et al., 2013; Menviel et al., 2014). Particularly, during MIS 2 and MIS 4 glacial conditions, the vegetation in the Guiana basin was characterized by savanna-type ecosystems (van der Hammen and Absy, 1994) whereas the sea surface temperature and the atmospheric temperature were ~4°C lower than present (van der Hammen and Absy, 1994; Nace et al., 2014; Rama-Corredor et al., 2015). It is thought that during the ice age, the NE trade winds were stronger generating a southward migration of the ITCZ and inducing drier climate conditions. Consequently, the sediment discharges delivered by rivers (Maroni, Orinoco) decreased in the Guiana basin due to low precipitation rates. Conversely, the Amazonian basin became wetter enhancing sediment fluvial discharge from the Amazon River (Arz et al., 1998; Arz et al., 1999; Mosblech et al., 2012). The hydrological activity of Maroni and the Orinoco was more important during the interglacial, as consequence of the ITCZ northward migration, when the Amazon basin turned into drier conditions.

D. Materials and methods

I. Studied cores

Three cores collected during the IGUANES cruise (2013, http://dx.doi.org/10.17600/13010030) are studied in this work (Fig. 2):

- IG-KSF-05 (at 08°02.80 N and 052°23.19 W, 3014 m water depth, 7 m in length), located in the contouritic drift and most likely characterized by a continuous sediment deposition. It is made of homogeneous grey-greenish mud with interbedded sandy intervals (Fig.3).

- IG-KSF-11 (at 07°51.85 N and 052°29.25 W, 2370 m of water depth, 6 m in length), located in the moat that follows the headscarp slope failure, where the current influence is the strongest. This core is composed of grey-greenish mud containing scattered sandy lenses (Fig.4).
- IG-KSF-15 (at 07°27.98 N and 052°19.76 W, 2578 m of water depth, 5 m in length), located in the moat same as IG-KSF-11 but located inside a comet mark shape depression. The core made of grey-greenish mud rich in green sandy grains with several carbonated-rich intervals interbedded (Fig.5).

II. Sediment analyses

Visual descriptions on split cores were performed to identify sedimentary facies. The sandy fraction (> 63 µm) was separated by wet sieving for observation under the microscope in order to quantitative evaluating the sand composition.

Grain-size analyses were performed on bulk sediment using a Malvern Mastersizer 3000 with a Hydro EV wet sample disperser associated with Mastersizer application software v3.60 on a 1 cm step sampling resolution for core IG-KSF-11 (Fig.4). Two series of measurements were generated: in bulk and carbonate-free sediment fractions. All samples (bulk sediment and carbonate-free) were placed in a solution of sodium metaphosphate ($NaPO_3$) at 1.5 g/L to deflocculate clay minerals. The distribution of size particles are used as an indicator of the winnowing effect (McCave et al., 1995; McCave and Hall, 2006).

Semi-quantitative geochemical analyses (element count rates) were performed along core IG-KSF-11 with an Avaatech X-Ray Fluorescence (XRF) core scanner (IFREMER, Brest) operated at both 10 kV and 30 kV and with a 1 cm sampling interval. In this study, Ca has been used to provide information about the biogenic components.

III. Glauconite study; quantification and analyses

The quantification of glauconitic grains was carried out on the sandy fraction every 10 cm in cores IG-KSF-11 (Fig. 4) and IG-KSF-15 (Fig. 5). The glauconitic grains were isolated under the microscope. Those were weighed and the weight was normalized with respect to 1) the sandy fraction and 2) the bulk sediment and then expressed as a percentage (%).The glauconitic grains were classified into three colour categories: yellowish-green, green, and dark green (visual estimation), the last one being sub-divided into dark and very dark green Representative samples were selected on core IG-KSF-11 for SEM observation, using a SEM HITACHI S-4500. These samples (104 grains) were collected at different intervals on IG-KSF-11: 0 cm, 50 cm, 270 cm, 300 cm, 450 cm, 460 cm and 590 cm. Quantitative elementary analyses were performed using a SEM-EDS system. Two measurements were carried out at the surface of each grain. These samples were collected at different intervals on IG-KSF-11: 50 cm, 270 cm, 300 cm, 450 cm, 460 cm and 590 cm. To complete this study, 9 additional samples on the 0 and 100 cm interval on IG-KSF-11 and one on the top of IG-KSF-15) were analysed for X-ray diffraction (Philips) on the < 2 µm fraction for clay minerals.

Four thin sections from indurated sediment were obtained in the IG-KSF-11, following the method described by Zaragosi et al. (2006). The selected intervals are: 20-40 cm; 337-367 cm; 449-479 cm; 580-600 cm (glauconite rich horizons). Thin sections have been observed under transmitted polarizing microscope for micro-facies description.

IV. Chronostratigraphy

Radiocarbon dates in different cores (IG-KSF-05 and IG-KSF-11) were obtained by Accelerator Mass Spectrometry (AMS) at the Poznań Radiocarbon Laboratory, using monospecific assemblages of well-preserved planktic foraminifer *Globigerinoides sp.* Measured ages were converted to calendar years using Calib 7.0.4 with the Marine 09 calibration curve (Reimer et al., 2013).

Oxygen stable isotope ratios were measured on samples from cores IG-KSF-11 and IG-KSF-05 using a 5 cm sampling step. These measurements were carried out on benthic (*Uvigerina mediterranea*) and planktonic (*Globigerinoides ruber* and *Globigerinoides sp.*) foraminifera at the Leibniz Laboratory for Radiometric Dating and Stable Isotope Research (Kiel, Germany).

Magnetic parameters allow an identification of the magnetic field at the time of sediment. NRM and isothermal remanent magnetization (IRM) measurements were made on cores IG-KSF-05 and IG-KSF-11, on U-channels (at 2 cm intervals) with a horizontal 2G Entreprises pass-through cryogenic magnetometer. NRM was demagnetized with an AF up to 80 mT using the in-line mounted alternating field (AF) demagnetizer. IRM was introduced in 1 T and -0.3 T fields, and the S-ratio ($IRM_{-0.3T}/IRM_{1T}$) was calculated.

E. **Results**

I. Chronostratigraphy

A multiproxy study was necessary to establish a chronostratigraphic framework. The steps followed for establishing a depth-age profile are described below, together with comments about the difficulties encountered.

1. Radiocarbon data

<u>IG-KSF11:</u>

In core IG-KSF-11 from 0 to 190 cm depth the ^{14}C ages range from 14 kyr BP to 50 kyr BP (Table 1), without any anomaly. The sediment accumulation rates calculated for this interval are:

- 0 - 60 cm: 2.7 cm/kyr
- 60 - 130 cm: 23 cm/kyr
- 130 - 190 cm: 5.5 cm/kyr.

The first stratigraphically incoherent age occurs at 313 cm with 43 kyr cal BP, followed by the 530 cm level, where two different ages are obtained (49 kyr BP and 26 kyr BP). The second measurement was performed on bulk sediment. Unfortunately, this material does not contain enough organic matter for accurate dating. Other stratigraphically incoherent ages are found at the bottom of the core at 582 cm (39 kyr BP) and 600 cm (28 and 35 kyr BP). The base of the core (600 cm) was measured twice and the resulting ages are largely different with a gap of 7 kyr.

IG-KSF-05:

The upper part of core IG-KSF-05 (0 cm) is dated at 5.6 kyr BP. The ages obtained deeper range from 44 kyr to 5.6 kyr (table 1) and give the following sediment accumulation rates:

- 0 – 29 cm: 2.4 cm/kyr
- 29 – 50 cm: 1.2 cm/kyr
- 50 – 169 cm: 33.9 cm/kyr

Some stratigraphic incoherencies are also present in this deeper part of the core (Table 1): 37.9 kyr BP at 169 cm, 30.6 kyr BP at 250 cm, 44 kyr BP at 340 cm and 41 kyr BP at 490 cm.

Thus, the stratigraphic incoherence and the strong difference in the sedimentation rates highlight the anomaly of dating, especially in the lower part of the two cores.

2. Stable isotopes and chronostratigraphy

Tie points have been identified comparing the relative oxygen isotope variations in the two cores studied in this work (Fig.6, table 2), in order to correlate them with Marine Isotope Stages (MIS).

The regional curves used here as references are (Fig.6):

1) oxygen isotope ratios from core MD03-2616 recovered in the Guiana Basin at a water depth of 1233 m and published in López-Otálvaro et al. (2009);

2) the Atlantic Ocean compilation from Lisiecki and Raymo (2005), (2009);
3) oxygen isotope ratios from core GeoB 3104 from a water depth of 767 m in the North Brazilian margin (Arz et al., 1998).

- **MIS 1 (0-11.7 kyr):** The core-tops of IG-KSF-11 and IG-KSF-05 (0 cm) do not correspond to modern ages, possibly because the upper part of the sediment column was lost during coring. A rapid increase of $\delta^{18}O$ values is observed at 10 cm depth in core IG-KSF-11 and at 18 cm depth in core IG-KSF-05, which can correlate with the beginning of MIS 1.
- **MIS 2 (11.7-24.1 kyr):** Between 10 and 43 cm with a sedimentary accumulation rate of 2.7 cm/10^3 yr in core IG-KSF-11 and 18 and 139 cm with a rate of 9.2 cm/10^3 yr in core IG-KSF-05, relatively high positive $\delta^{18}O$ values are thought to correspond to the MIS 2 cold stage. The low resolution of the isotope measurements does not allow us to precisely identify the glacial maximum, but the correlation with Arz et al. (1998) isotope curve, suggests that the LGM could be positioned at 20 cm depth in IG-KSF-11 and at 35 cm depth in IG-KSF-05 (Fig.6);
- **MIS 3 (24.1-58.9 kyr):** The interval comprised between 43 and 80 cm in IG-KSF-11 (1 cm/10^3 yr) and between 139 and 451 cm in IG-KSF-05 (8.7 cm/10^3 yr) is tentatively assigned to MIS 3. However, its features cannot be directly compared to the global curves (Fig.6), mainly because of the occurrence of relatively negative values obtained in planktonic and benthic foraminifera in both cores (Fig.6). These oscillations are not evident at the global scale but are nonetheless observed regionally, as illustrated in López-Otálvaro et al. (2009);
- **MIS 4 (58.9-74 kyr):** This (moderate) glacial stage is located in the 80-150 cm interval in core IG-KSF-11 (4.6 cm/10^3 yr) and in the 451-590 cm interval in core IG-KSF-05 (9.2 cm/10^3 yr), based on the relative $\delta^{18}O$ variations compared to MIS 3

(Fig.6). The pattern of isotope ratio values is considered coherent and comparable with the global temperature trends;

- **MIS 5 (74-130 kyr):** The interval between 150 and 267 cm in IG-KSF-11 and 590 and 694 cm in IG-KSF-05 is assigned to MIS 5. The MIS 5 is subdivided into five sub-stages (MIS 5.1 to MIS 5.5) that are recorded in many areas of the ocean (Shackleton et al., 2003) where the MIS 5.5 consists in the most prominent temperature rise (Fig.6). In core IG-KSF-11, two intervals show considerably negative $\delta^{18}O$ values (at 160-200 cm depth and 235-365 cm depth, Fig.6) that could possibly match the MIS 5.1 and 5.3. Thus, the basal prominent peak would be missing. The reason why it is lacking is not clear, but a non-depositional or even an erosional episode is possible.
- **MIS 6 (130-189.6 kyr) and MIS 7 (189.6-244 kyr)?:** Below MIS 5, the correlation becomes really uncertain. A possible assignment of the interval comprised between 267 and 371 cm in core IG-KSF-11 to MIS 6 is proposed, since the relatively positive $\delta^{18}O$ values might be consistent with a glacial stage (Fig.6), but there is no other proxy that could confirm this hypothesis. Even more difficult is the interpretation of the interval below 380 cm depth in core IG-KSF-11 (Fig.6) since it is possibly affected by heavy reworking. In an optimistic view, it could be possible to consider that the interval comprised between 371 and 422 cm depth might belong to MIS 7, but with no certitude. On the other hand, below 430 cm depth, the sediment is fully reworked. The question, which remains open in this work, is when this reworking took place, either during the glacial stage (MIS 8), the interglacial (MIS 7), or later.

3. Palaeomagnetism

As shown by Bleil and Von Dobeneck (1999), the natural remanent magnetization (NRM) can record the direction (declination and inclination), the relative palaeointensity and the geomagnetic event during the Late Quaternary. In marine environments, the ferromagnetic detrital minerals such as magnetite and hematite become aligned by the geomagnetic field as they fall through the water and become part of the sediment on the bottom of the sea; it is the detrital remanent magnetization (DRM) that often contributes predominately to the NRM in such marine sediments.

In the cores IG-KSF-11 and IG-KSF-05, the NRM decrease during the demagnetisation and the S-ratio values varying between 0.9 and 0.8 indicate that the magnetic fraction of the sediment is dominated by minerals of low coercivity such as magnetite, with minor amounts of higher coercivity minerals - hematite or goethite (Tudryn et al., 2010). In the bottom (600 - 450 cm depth) of the core IG-KSF-11, slightly lower S-ratio values (0.7 - 0.8) indicate increased contents of the hematite and/or goethite. NRM shows stability in direction and low inclination values, except in the bottom of the core IG-KSF-11 (Fig. 4) and the top of IG-KSF-05 (Fig. 3). On the top of the core IG-KSF-05, an important variation in declination and inclination is recorded around the transition between MIS 1 (0-18 cm) and MIS 2 (25-139 cm) as identified through $\delta^{18}O$ record (above); it likely corresponds to the Gothenburg Geomagnetic Polarity Excursion at 12.5 kyr (Mörner, 1977; Barbetti et al., 1980; Mörner, 1986), described between 12.5 and 13.5 kyr in European and Cameroon lakes (Smith and Creer, 1986; Thouveny and Williamson, 1988; Maley et al., 1990). The Laschamp event, around 40 kyr (Bonhommet and Babkine, 1967; Guillou et al., 2004; Plenier et al., 2007), and the Blake event, around 119 kyr (Lund et al.; Smith and Foster, 1969; Gibbard and Cohen, 2008), seem to be absent or not identifiable in the studied successions. Nonetheless, the stability of magnetic parameters suggests that the sediment was not affected by post-depositional reworking, except for the basis of IG-KSF-11 and probably the top of IG-KSF-05.

II. Grain size analysis

In the core IG-KSF-11 (Fig.4), the average clay content is 20% of the total sediment, while the fine silt-size fractions account for between 40 and 60% and hence constitute the dominant fraction. Coarse silt and sand correlate to Ca relative content suggesting that this relatively coarse fraction is made of biogenic carbonates, relatively abundant during estimated ice periods (MIS 2-4-6; Fig.4).

The free carbonate $\overline{SS}$ varies between 15 µm and 30 µm (Fig.4). With respect to the bulk sediment grain-size plot, the $\overline{SS}$ is high between 420-600 cm and the bottom of the core. The values increase during the ice period MIS 6 (267-371 cm) and decrease to relatively low values during MIS 5 (150-267 cm). Some higher values correspond to the 200-230 cm interval and are associated with an increase in isotopic values. The $\overline{SS}$ becomes high from MIS 4 and through the 'weak' MIS 3 interglacial (Fig.4).

III. Facies

1. Analysis

Seven sedimentary facies have been identified after visual description of all cores (Tallobre, 2017), combined with observations of thin sections on core IG-KSF-11 (Table 3). They are described as follows:

- **F1 Carbonate facies** with indurated foraminifera-rich carbonate (Table 3, Fig.5). This F1 corresponds to remobilized sediment blocks, which are dated to the Oligocene-Miocene period (Tallobre, 2017). This slope instability event has also been described further Northwest by Ingram et al. (2011).
- **F2 Glauconitic sand** composed by glauconitic sand (20-30%) and biogenic debris (mainly foraminifera). Glauconitic grains are dominant and constitute up to 94% of the sandy fraction (Table 3, Fig.7A- 7B-8C). Laminae, sand lenses and bioturbation can be

observed. Glauconite can (1) infill foraminifer tests whose the moulds can be preserved (Fig.7B, 8C) or (2) form infra-millimetric clasts (Fig.7C-7F). The latter show a high degree of fracturing, irregular shape and they can derive from erosion and transport of slightly lithified glauconitic beds hardground.

- **F3 Sandy facies.** It is characterized by bioturbated foraminifera-rich sand mixed with glauconitic grains (between 0.1% and 1% of highly fractured glauconite grains in the sandy fraction, and around 20 % of sand and coarse silt) and joined grains as illustrated on the thin section (Table 3, Fig.7C-8E). Laminae or sand lenses can be found (Fig.7C).
- **F4 Foraminifera- and glauconitic-bearing muddy facies** with slightly laminated foraminifera rich mud (Table 3), few glauconitic grains (with a proportion lower of 0.1%) in the sand fraction (Fig.7D-8D). It can be differentiated from F3 because of the low content of sandy grains and because glauconitic grains are less abundant in the mud and concentrated in bioturbation (Fig. 8A-8B).
- **F5 Foraminifera sand** composed by foraminiferal sandy facies (20% of sand and coarse silt) with joined grains and poor in glauconitic grains (Table 3, Fig.7E). The fracturing of grains is moderate to low.
- **F6 Foraminifera-bearing muddy facies** similar to F5, (rich in foraminifera and rare glauconitic grains). The distinctive difference lies in the proportion of sandy grains (Table 3) that are diluted in the mud and not joined (Fig.7F).
- **F7 Muddy facies** composed by massive mud (Table 3, Fig.7G) with low foraminifera and rare glauconitic grains.

2. Comments

Some of the described facies record contrasted hydrodynamic conditions and may correspond to a local expression of the ideal contouritic sequence. In particular:

- F2 Glauconitic sand and F3 Sandy facies, based on grain size and grain fracturing, associated to degraded organic matter (Tallobre et al., 2016), are characteristic of high winnowing conditions and may correspond to an equivalent of the C3 contourite sequence.
- F4 Foraminifera- and glauconitic-bearing muddy facies, poorer in sandy grains may relate to the upper part of C2 with an increasing winnowing effect, whereas the lower part of C4 should correspond to decreasing winnowing effect.
- F5 Foraminifera sand and F6 Foraminifera-bearing muddy facies, with quite abundant foraminifera tests (the sandy fraction) may correlate to the lower part of C2 and the upper part of C4 and a moderate winnowing effect.
- Finally, F7 Muddy facies, the finest in terms of grain size, probably corresponds to an equivalent of units C1 and C5. The good organic matter preservation in this facies is consistent with very low winnowing effect (Tallobre et al., 2016).

IV. Glauconite study

1. Glauconitic grain facies and contents

Sediments collected in the moat are rich in glaucony (Fig.4-5). On the contrary, sediment from the contouritic drift, as IG-KSF-05 (Fig.3), contain less glauconitic grains and sometimes abundant pyrite can be found (usually anti-correlating the glauconite content).

a. *Core IG-KSF-11*

Vertical distribution of glauconitic grains for IG-KSF-11 (Fig.4) has been compared to $\delta^{18}O$ ratios for correlation with the glacial/interglacial intervals previously defined:

- Between 500-601 cm (chronologically undefined interval), the sediments have a moderate content in glauconitic grains (0.08% on average for the bulk sediment), with

17% of yellowish-greenish, 42% of green and 41% of dark green grains (with the green shade illustrated in Fig.4);

- Between 400 and 500 cm (reworked and chronologically undefined interval two high glauconitic grain content peaks stick out (430-440 cm and 480-490 cm): 11% and 13% in the bulk sediment and 94% and 91% in the sandy fraction (facies F2). The dark green grains represent 95-96% of glauconitic grains;
- In sediment corresponding to glacial stages (10-43 cm in MIS 2, 80-150 cm in MIS 4 and 267-371 cm in MIS 6), the green grain content is moderate (facies F3-F4) to high (facies F2). This is particularly true in the MIS 6 sediments where the green grain content reaches 1.2% in bulk sediment and 25% of the sandy fraction. Yellowish-greenish grains are less abundant (up to 15% in the 267-371 cm interval), whereas green grains and dark green grains reach high concentrations (50% and 40%, respectively). As a general trend, the abundance of glauconitic grains decreases upward from the beginning of the glacial stage (Fig.4).
- The interglacial periods (43-80 cm in MIS 3, 150-267 cm in MIS 5, and part of MIS 7 at 371-400 cm) are characterized by low glauconitic contents (sometimes completely absent, facies F6-F7). When glauconitic grains are present, they are generally yellowish to greenish. The Holocene (0-10 cm) yields moderate glauconitic content of 0.04 to 0.09% of the bulk sediment (50% of green and dark green grains, with up to 80% of dark green at the top of the core).

b. *Core IG-KSF-15*

In core IG-KSF-15 (Fig.5), the interval between170-470 cm is composed of an alternation of silty-clay and silty-sandy beds, all rich in glauconitic grains with 47% of dark green and 26% of green grains corresponding to facies F2. The interval corresponding to 120-170 cm is made of carbonated reworked sediment (facies F1). Although some glauconitic grains are present between 170-160 cm, the glauconitic concentration remains poor. The top of the core (0-120 cm) is characterized by fine sediments with low content in glauconitic grains (facies F4) and 50% of yellowish-greenish grains.

2. SEM observations and microprobe analysis on glauconitic grains

Under the SEM observation, it has been possible to correlate the increasing colour darkness to the presence of cracks at the surface of the grain (Fig.9). These cracks become more abundant and deeper as the grains get darker. Micro-sheets are also observed, more numerous and more distinct as the green colour becomes darker. They can eventually form a 'rose' structure (Fig.9). These neo-formed sheets gradually fill the intra-grain porosity.

Elementary analyses were performed and compared for the four colour categories of glauconitic grains visually defined. The averages of results for major element compositions are presented in table 4. The reference mud samples collected correspond to beds with less than 0.1% of green grains. In the mud, the high value in Al_2O_3 suggests the occurrence of kaolinite, but this oxide can also be found too in illite and smectite. The Mg is generally found in smectite, and to a lesser extent in illite.

On the basis of the obtained results, hereafter the points that can be highlighted:

- Marine mud, on the top of core IG-KSF-11, analysed by X-Ray diffraction, is composed by 25% of smectite, 35% of illite and 40% of kaolinite. The content in Al_2O_3 is 18.1%, 9% for Fe_2O_3, and 2.5% for K_2O (Fig.10).
- In greenish/yellowish grains, the content in Al_2O_3 decreases at 8.8%, whereas it increases for Fe_2O_3 to 27% and for K_2O to 2.9% (Fig.10).
- In green grains, the content in Al_2O_3 decreases again at 7.4%, the increasing keep up for Fe_2O_3 to 30.3% (and punctually until 33.4% on Fig.9) and for K_2O to 3.2% (Fig.10).

- The trend continues for dark green grains: decrease for Al_2O_3 at 5.6%, and increase for Fe_2O_3 to 34% and for K_2O to 4.3% (Fig.10).
- For very dark green grains, the content in Al_2O_3 (5.8%) and in Fe_2O_3 (34.2%) vary only slightly whereas the content in K_2O continue to progress in average to 5.8% (Fig 10) and punctually until 6.5% in K_2O (Fig.9).

The greening process is characterized by a rapid and strong increase of iron (Fig.10). The potassium also increases, more slowly and keeps up longer than iron.

F. Discussion

The main weak point in this study is the uncertain chronostratigraphic framework. It has been established by putting together information inferred from different proxy data but it is far from being perfect. Unfortunately, all possible dating methods (applicable to this site) do not allow 1) building a more precise age model; 2) to identify with precision the presence and duration of sediment hiatuses. The uncertainties remain significant, especially before MIS 5. Because of the impossibility of obtaining a better precision, we have limited the chronostratigraphy to the identification of glacial and interglacial stages proposing a correlation with isotope stages, as described in the paragraph 2, in order to describe the mechanisms at the origin of glauconite formation in the contourite sequences and their possible relation with climate. Despite the significant difficulty to establish a solid chronostratigraphic framework before MIS 5, the studied cores represent quite exceptional sediment archives for correlating the phenomenon of glauconite formation and to establish to what extends this feature can be used as a reliable proxy for paleoceanographic reconstructions.

I. Glauconitisation process

1. Formation and maturation of green grains

During glauconitisation, the enrichment in K (from 2.9% to 5.8% K_2O, Fig.9-10) and Fe (from 27% to 34.2% Fe_2O_3) occurs at different rates with glauconite maturation (table 4). The greening of grains expresses enrichment in Fe-smectite and interstratified Fe-smectite/glauconite. The diachronic evolution, between Fe and K, illustrates the fact that iron is incorporated and oxidized rapidly, whereas K assimilation is a slightly slower process (Fig.10 and table 4). This greening is characterized first, by Fe-smectite neoformation, and then, by neoformation of interlayered minerals. Incorporation of Mg, Fe and K in the mineral structure (Fig.9) is the way to transform smectite into Fe-smectite and then into interstratified Fe-smectite/glauconite. It expresses the chemical evidence of the maturation process of glauconitic grains (Odin, 1988; Giresse and Wiewióra, 2001; Wiewióra et al., 2001; Giresse, 2008; Baldermann et al., 2013; Baldermann et al., 2015; Banerjee et al., 2016).

Greening is controlled by the chemical evolution and oxidation state of Fe. Ferrous Fe is at the origin of the grains green colour and its oxidation in Fe-ferric is responsible for the darkening. The elementary composition is the indicator of mineralogical evolution phases (Fe-smectite, interstratified Fe-smectite/Glauconite, and glauconite). The chemical evolution, and thus the greening, are related to the development of numerous micro-sheets (illustrated on the SEM pictures on the Figure 9) infilling the intra-grain porosity. These characteristics indicate the maturity of glauconitic grains. The multiplication of Fe-smectite and interlayered micro-sheets (see SEM pictures on Fig.9) generates density variations (between original mud and the different mineralogical states (Giresse, 2008)). The greening process is associated with the neoformation of interstratified Fe-smectite/illite by the incorporation of K. The neoformed Fe-smectite, which are hydrated, are less dense. This growing neoformation of hydrated minerals causes the decrease of density and increase of volume. Hence, the neoformation generates a pressure inside green grains which induces cracking at the grain surface, well developed and clearly shown on the SEM pictures (Fig.9). These cracks are thus an indicator of the mineralogical maturity of glauconitic grains (Giresse, 2008).

2. Glauconitisation at the sea/surface interface

The analyses performed on green grains indicate a geochemical trend and that the greening is accompanied by elementary and mineralogical changes (Fig.9-10).

However, the limiting factor for glauconitisation is the availability of Fe (supplied by the alteration of minerals of continental origin) and K (directly provided by sea water). In the anoxic mud of deep-sea sediments, iron is mainly present as Fe^{2+}. The rapid oxidation of organic matter causes a redox front between the grain and the surrounding mud, making the micro-environment around the foraminifera more oxidising than the mud matrix (Odin, 1988; Giresse and Wiewióra, 2001; Wiewióra et al., 2001; Giresse, 2008). Thus, Fe^{2+} migrates rapidly inside foraminifera tests, where it is partly oxidized into Fe^{3+} and possibly incorporated into octahedral structures; smectites become Fe-smectites (Fig.10.1 and 10.2). This process occurs relatively rapidly at the water/sediment interface. In contrast to Fe, K migrates slowly and gradually from seawater into the micro-environment inside buried foraminifera tests below the seafloor to form glauconite assemblages (Fig.10). The interlayer incorporation of K, and consequently glauconitisation, requires a long exposure period at the sea water/sediment interface. If these two conditions are filled, the transformation of detrital clay minerals into Fe-smectite, interlayered Fe-smectite/glauconite and glauconite is possible (Fig.10). The formation of mature glauconitic grains, composed of Fe-smectites and interlayered Fe-smectite/glauconite (with 5% to 6.5% K_2O in our samples Fig.9), occurs rapidly during the early diagenetic process (about 10 to 100 kyr). The complete glauconitisation process (with more than 8% of K_2O expected (Giresse, 2008)) needs a longer period of time, ranging from 2 to 10 Myr (Odin and Fullagar, 1988; Odin, 1988; Gaudin et al., 2005; Baldermann et al., 2013), and as such often happens during late marine diagenetic processes.

3. Glauconitisation and winnowing effect

During early diagenesis, glauconitisation occurs at the water/sediment interface with low sedimentation rates to promote the incorporation of Fe and subsequently K (McRae, 1972; Odin, 1988; Giresse and Wiewióra, 2001; Wiewióra et al., 2001; Giresse, 2008). At times, low sedimentation rates can be induced by the winnowing effect linked to bottom current activity (Chafetz and Reid, 2000; Giresse and Wiewióra, 2001; Wiewióra et al., 2001; Giresse, 2008).

In Demerara contouritic sediments, the glauconitic facies (F2) are characterized by high sandy and silt content, high value of $\overline{SS}$, high fracturing of grains, and an enhanced degradation of organic matter (Tallobre et al., 2016). These elements suggest that the glauconitisation might be related to high winnowing effect. Moreover, the here described glauconitic facies corresponds to sediments collected in the moat (Fig.4-5) stronger bottom water winnowing) whereas this facies is absent in sediments collected in the drift (Fig.3, weaker bottom water winnowing, finer sediments and rare glauconite fracturing features).

As a consequence, we put forward the hypothesis that during the period characterized by the highest current intensity, the winnowing effect inhibits sediment deposition and instead causes erosion at the seafloor and high fracturing of foraminifers' tests. The mud directly in contact with seawater, is more oxidising than in the underlying mud, which can promote the occurrence of a redox front and, likely, glauconitisation (Fig.10).

Glauconitisation at the seafloor is concomitant to the formation of indurated beds. Occasionally, during the erosional phases, some coarse clasts can be reworked from the seafloor, deposited and mixed within the glauconitic sandy facies as intraclasts (facies F2, Fig. 8C-8F).

II. Glauconite and contourite sequence

The link between glauconitic grain maturity, winnowing effect and current intensity allows us to propose an alternative 'ideal' contouritic sequence that integrates the glauconite content and its degree of maturity (Fig.11). Thus, units C1 and C5 might correspond to low current velocity muddy facies, with a low glauconitic grain content and maturity (Fig.3 and 4). The C2 and C4 mottled muddy facies should record current velocity decrease and subsequent increase, corresponding to negatively and positively graded sediments. Those facies contain abundant glauconitic grains including a mixture of different green grains with dominance of dark green and light green grains. The dark green grain concentration increases with coarsening in C2, and it decreases in the fining upward of C4, and inversely for yellowish-greenish grains (Fig.3, 4 and 5). Finally, the C3 sandy facies corresponding to the maximum current velocity is characterized by a high content of dark green grains as illustrated along the cores (Fig.3, 4 and 5). At the maximum of bottom current intensity, during low sedimentation, hardground surfaces might form with possible erosion and formation of glauconitic intraclasts.

III. Winnowing effect and current velocity Quaternary evolution

While the evolution of the NADW intensity is still subject to discussion, the results obtained in this study for the Demerara Plateau (IG-KSF-11 and IG-KSF-05) provide further evidence on the factors that may have affected the strength of deep-ocean circulation and its effect on sedimentation in the equatorial western Atlantic. It is necessary to bear in mind that the chronostratigraphic framework obtained on the studied cores is not sufficiently robust for being considered conclusive. However, based on the $\delta^{18}O$ relative variations and palaeomagnetic records, we propose the distinction between glacial vs interglacial intervals in these cores, in order to discuss the evolution of bottom currents according to climate conditions.

To resume the features observed in the sediments, the glacial stages are characterised by:

- relative high glauconitic grain content;
- high maturity of glauconitic grains;
- sandy facies, rich in sand and coarse silt;
- high degree of fracturing of the shell debris and glauconitic grains;
- largely winnowed organic matter.

Within the intervals corresponding to the full interglacials, it is possible to observe:

- moderate to very low glauconitic content,
- low maturity of glauconitic grains,
- muddy facies, rich in clays and fine silt
- low degree of fracturing of shells,
- better preservation of organic matter.

Taken together, the observed differences between glacial and interglacial sediment characteristics suggest that global climate exerts a strong control on contourite deposition and associated diagenetic processes. Evidence of a high winnowing effect, which coincided with low sedimentation rates caused by a high current velocity, would be consistent with the hypothesis of a vigorous bottom current activity during the glacial periods (Curry and Oppo, 2005; Böhm et al., 2015; Lippold et al., 2016).

Particularly, the degree of glauconite maturity in the cores studied in this work, suggests the presence of an active overturning circulation during the glacial phases in this segment of Atlantic Ocean. Lippold et al. (2016) evidenced the persistence of a vigorous oceanic circulation during the LGM in the relatively shallow (>2000 m depth) Southern Atlantic, but the case of Demerara Plateau is even more peculiar, because of its particular morphology. As stated before, the large indentation is thought to be at the origin of the intensification of the NADW, favouring the formation of contourites (Tallobre et al., 2016). Here, we put forward the hypothesis that during glacial stages, the action of overturning circulation could have been amplified by the Demerara Plateau morphology, inducing a strong and prolonged winnowing on sediments as testified by the glauconite neoformation.

G. **Conclusion**

This study describes the characteristics of deposits belonging to contourite sequences on the Demerara Plateau, through the detailed analyses of sediment cores retrieved during the IGUANES cruise. A very distinctive sediment feature is the presence of an authigenic mineral, the glauconite, that here is thought to be formed under the effect of bottom water hydrodynamic conditions, since the formation of glaucony might be relatively rapid at the water/sediment interface during the first stage of diagenesis.

In particular, the winnowing effect is very likely at the origin of the formation of glauconite (composed of Fe-smectite and interlayered Fe-smectite/glauconite) that is observed to develop mainly inside foraminifera tests at the sediment-water interface.

The detailed study of glauconite grains allowed to identify the different phases of the glauconitisation process, and characterized by (1) increasing relative abundance of glauconitic grains and (2) increasing degree of mineralogical maturity.

The degree of maturity has been defined by (a) grain colour (yellowish green for immature glauconite to dark green for very mature glauconite), (b) the presence of cracks at the grain surface, together with the enrichment in neoformed microstructures and decreasing porosity inside grains and (c) by mineralogical and chemical composition change. The formation of glaucony is relatively rapid at the water/sediment interface during the first stage of diagenesis.

Hence, the features of glauconitic grains are here used as an indicator of the winnowing effect. This *proxy* is thought to have a good potential since it allows a semi-quantitative estimation of the current intensity and, combined with other sedimentological and geochemical parameters, could have an interest in studies of contouritic deposits.

In this study, the characteristics of glauconitic sediments and their correlation with the major climate shifts, suggest that the NADW flow was strengthened during glacial periods, likely because the local morphology (indentation of the Demarara Plateau) may have generated a strong and prolonged bottom water winnowing.

H. Acknowledgments

The authors would like to thank the crew of the N/O L'Atalante. We also thank Shell and Ifremer for supporting Cédric Tallobre's PhD Project, Ifremer Brest laboratories for technical support on sediment core handling and analyses (Angélique Roubi, Mikael Rovere, Joël Etoubleau); Bernard Martin at the University of Bordeaux the thin sections; the CEFREM (University of Perpignan), Christophe Menniti, Bruno Charrière, Jennifer Sola, Stéphane Kunesch, Christine Sotin for access to laboratory facilities and assistance. Many thanks to the graduate students who worked on this topic: Camille Ferrer, Lea Bonnin, Simon Faye, Emmanuel Chassagnac. Finally, authors thank reviewers and editors for their contributions to improve this paper.

I. References

Arz, H.W., Pätzold, J., Wefer, G., 1998. Correlated Millennial-Scale Changes in Surface Hydrography and Terrigenous Sediment Yield Inferred from Last-Glacial Marine Deposits off Northeastern Brazil. Quaternary Research 50, 157-166.

Arz, H.W., Pätzold, J., Wefer, G., 1999. Climatic changes during the last deglaciation recorded in sediment cores from the northeastern Brazilian Continental Margin. Geo-Marine Letters 19, 209-218.

Bahk, J.J., Chough, S.K., Jeong, K.S., Han, S.J., 2001. Sedimentary records of paleoenvironmental changes during the last deglaciation in the Ulleung Interplain Gap, East Sea (Sea of Japan). Global and Planetary Change 28, 241-253.

Bahk, J.J., Lee, S.H., Yoo, H.S., Back, G.G., Chough, S.K., 2005. Late Quaternary sedimentary processes and variations in bottom-current activity in the Ulleung Interplain Gap, East Sea (Korea). Marine Geology 217, 119-142.

Baldermann, A., Deditius, A.P., Dietzel, M., Fichtner, V., Fischer, C., Hippler, D., Leis, A., Baldermann, C., Mavromatis, V., Stickler, C.P., Strauss, H., 2015. The role of bacterial sulfate reduction during dolomite precipitation: Implications from Upper Jurassic platform carbonates. Chemical Geology 412, 1-14.

Baldermann, A., Warr, L.N., Grathoff, G.H., Dietzel, M., 2013. The rate and mechanism of deep-sea glauconite formation at the ivory coast–ghana marginal ridge. Clays and Clay Minerals 61, 258-276.

Banerjee, S., Bansal, U., Vilas Thorat, A., 2016. A review on palaeogeographic implications and temporal variation in glaucony composition. Journal of Palaeogeography 5, 43-71.

Barbetti, M., Taborin, Y., Schmider, B., Flude, K., 1980. Archaeomagnetic results from late Pleistocene hearths at Etiolles and Marsangy, France. Archaeometry 22, 25-46.

Bleil, U., Von Dobeneck, T., 1999. Geomagnetic events and relative paleointensity records—Clues to high-resolution paleomagnetic chronostratigraphies of Late Quaternary marine sediments?, Use of proxies in paleoceanography. Springer, pp. 635-654.

Böhm, E., Lippold, J., Gutjahr, M., Frank, M., Blaser, P., Antz, B., Fohlmeister, J., Frank, N., Andersen, M., Deininger, M., 2015. Strong and deep Atlantic meridional overturning circulation during the last glacial cycle. Nature 517, 73-76.

Bonhommet, N., Babkine, J., 1967. Sur la presence d'aimantations inversees dans la Chaine des Puys. Comptes rendus hebdomadaires des seances de l academie des sciences serie b 264, 92-94.

Chafetz, H.S., Reid, A., 2000. Syndepositional shallow-water precipitation of glauconitic minerals. Sedimentary Geology 136, 29-42.

Curry, W.B., Oppo, D.W., 2005. Glacial water mass geometry and the distribution of δ13C of ΣCO2 in the western Atlantic Ocean. Paleoceanography 20.

Faugères, J.-C., Gonthier, E., Stow, D.A.V., 1984. Contourite drift molded by deep Mediterranean outflow. Geology 12, 296-300.

Faugères, J.-C., Zaragosi, S., Mézerais, M., Massé, L., 2002. The Vema contourite fan in the South Brazilian basin. Geological Society, London, Memoirs 22, 209-222.

Faugères, J.C., Mulder, T., 2011. Contour Currents and Contourite Drifts. in: Heiko Hüneke and Thierry Mulder, Deep sea sediments, elseiver publications, developments in sedimentology 63, 149-205.

Gaudin, A., Buatier, M., Beaufort, D., Petit, S., Grauby, O., Decarreau, A., 2005. Characterization and origin of Fe3+-montmorillonite in deep-water calcareous sediments (Pacific Ocean, Costa Rica margin). Clays and Clay Minerals 53, 452-465.

Gaullier, V., Loncke, L., Droz, L., Basile, C., Maillard, A., Patriat, M., Roest, W.R., Loubrieu, B., Folens, L., Carol, F., 2010. Slope instability on the French Guiana transform margin from swath-bathymetry and 3.5 kHz echograms, Submarine Mass Movements and Their Consequences. Springer, pp. 569-579.

Gibbard, P., Cohen, K.M., 2008. Global chronostratigraphical correlation table for the last 2.7 million years. Episodes 31, 243-247.

Giresse, P., 2008. Chapter 12 Some Aspects of Diagenesis in Contourites, In: Rebesco, M., Camerlenghi, A. (Eds.), Developments in Sedimentology. Elsevier, pp. 203-221.

Giresse, P., Wiewióra, A., 2001. Stratigraphic condensed deposition and diagenetic evolution of green clay minerals in deep water sediments on the Ivory Coast–Ghana Ridge. Marine Geology 179, 51-70.

Gonthier, E., Faugères, J.C., Stow, D.A.V., 1984. Contourite facies of the Faro drift. Geological society of London, special publication 15, 275-292.

Guillou, H., Singer, B.S., Laj, C., Kissel, C., Scaillet, S., Jicha, B.R., 2004. On the age of the Laschamp geomagnetic excursion. Earth and Planetary Science Letters 227, 331-343.

Heezen, B.C., 1959. Dynamic Processes of Abyssal Sedimentation: Erosion, Transportation, and Redeposition on the Deep-sea floor. Geophysical Journal International 2, 142-163.

Heezen, B.C., Hollister, C., 1964. Deep-sea current evidence from abyssal sediments. Marine Geology 1, 141-174.

Heezen, B.C., Johnson, G.L., 1963. A moated knoll in the Canary Passage. Dent. Hydrograph. Z. 16, 269-272.

Hernández-Molina, F.J., Paterlini, M., Violante, R., Marshall, P., de Isasi, M., Somoza, L., Rebesco, M., 2009. Contourite depositional system on the Argentine Slope: An exceptional record of the influence of Antarctic water masses. Geology 37, 507-510.

Hurley, P., Rand, J., Pinson, W., Fairbairn, H., de Almeida, F., Melcher, G., Cordani, U., Kawashita, K., Vandoros, P., 1967. Test of Continental Drift by Comparison of Radiometric Ages A pre-drift reconstruction shows matching geologic age provinces in West Africa and Northern Brazil. Science 157, 495-500.

Ingram, W.C., 2006. Anatomy of Oligocene-Miocene debris flow and slumps form Demerara Rise: implications for margin destruction American Association of Petroleum Geologists 2006 annual Convention, Houston.

Ingram, W.C., Mosher, D.C., Wise, S.W.J., 2011. Biostratigraphy of an upper Miocene mass transport deposit on Demerara Rise, northern South American margin, In: Shipp, C., Weimer, P., Posamentier, H. (Eds.), Mass-transport Deposits in Deepwater Settings. SEPM Special Publication 96, pp. 457-498.

Kageyama, M., Merkel, U., Otto-Bliesner, B., Prange, M., Abe-Ouchi, A., Lohmann, G., Ohgaito, R., Roche, D., Singarayer, J., Swingedouw, D., 2013. Climatic impacts of fresh water hosing under Last Glacial Maximum conditions: a multi-model study. Climate of the Past 9, 935-953.

Lee, S.H., Bahk, J.J., Chough, S.K., Back, G.G., Yoo, H.S., 2004. Late Quaternary sedimentation in the Ulleung Interplain Gap, East Sea (Korea). Marine Geology 206, 225-248.

Lippold, J., Gutjahr, M., Blaser, P., Christner, E., de Carvalho Ferreira, M.L., Mulitza, S., Christl, M., Wombacher, F., Böhm, E., Antz, B., 2016. Deep water provenance and dynamics of the (de) glacial Atlantic meridional overturning circulation. Earth and Planetary Science Letters 445, 68-78.

Lisiecki, L.E., Raymo, M.E., 2005. A Pliocene-Pleistocene stack of 57 globally distributed benthic δ18O records. Paleoceanography 20.

Lisiecki, L.E., Raymo, M.E., 2009. Diachronous benthic δ18O responses during late Pleistocene terminations. Paleoceanography.

Loncke, L., Droz, L., Gaullier, V., Basile, C., Patriat, M., Roest, W., 2009. Slope instabilities from echo-character mapping along the French Guiana transform margin and Demerara abyssal plain. Marine and Petroleum Geology 26, 711-723.

Loncke, L., Maillard, A., Basile, C., Roest, W.R., Bayon, G., Gaullier, V., Pattier, F., Mercier de Lépinay, M., Grall, C., Droz, L., Marsset, T., Giresse, P., Caprais, J.C., Cathalot, C., Graindorge, D., Heuret, A., Lebrun, J.F., Bermell, S., Marcaillou, B., Sotin, C., Hebert, B., Patriat, M., Bassetti, M.A., Tallobre, C., Buscail, R., Durrieu de Madron, X., Bourrin, F., 2016. Structure of the Demerara passive-transform margin and associated sedimentary processes. Initial results from the IGUANES cruise. Geological Society, London, Special Publications 431.

Lopes, R.P., Kinoshita, A., Baffa, O., Figueiredo, A.M.G., Dillenburg, S.R., Schultz, C.L., Pereira, J.C., 2014. ESR dating of Pleistocene mammals and marine shells from the coastal plain of Rio Grande do Sul state, southern Brazil. Quaternary International 352, 124-134.

López-Otálvaro, G.-E., Flores, J., Sierro, F., Cacho, I., Grimalt, J.-O., Michel, E., Cortijo, E., Labeyrie, L., 2009. Late Pleistocene palaeoproductivity patterns during the last climatic cycle in the Guyana Basin as revealed by calcareous nannoplankton. EEarth 4, 1-13.

Lund, S.P., Schwartz, M., Keigwin, L., Redefinition of the Blake Event.

Maley, J., Livingstone, D.A., Giresse, P., Thouveny, N., Brenac, P., Kelts, K., Kling, G., Stager, C., Haag, M., Fournier, M., Bandet, Y., Williamson, D., Zogning, A., 1990. Lithostratigraphy, volcanism, paleomagnetism and palynology of Quaternary lacustrine deposits from Barombi Mbo (West Cameroon): Preliminary results. Journal of Volcanology and Geothermal Research 42, 319-335.

McCave, I., Manighetti, B., Robinson, S., 1995. Sortable silt and fine sediment size/composition slicing: parameters for palaeocurrent speed and palaeoceanography. Paleoceanography 10, 593-610.

McCave, I.N., Hall, I.R., 2006. Size sorting in marine muds: Processes, pitfalls, and prospects for paleoflow-speed proxies. Geochemistry, Geophysics, Geosystems 7, 1-37.

McRae, S.G., 1972. Glauconite. Earth-Science Reviews 8, 397-440.

Menviel, L., Timmermann, A., Friedrich, T., England, M., 2014. Hindcasting the continuum of Dansgaard–Oeschger variability: mechanisms, patterns and timing. Climate of the Past 10, 63-77.

Mercier de Lépinay, M., Loncke, L., Basile, C., Roest, W., Patriat, M., Maillard, A., De Clarens, P., 2016. Transform continental margins - Part 2: A worldwide inventory. Tectonophysics.

Mörner, N.-A., 1977. The Gothenburg Magnetic Excursion. Quaternary Research 7, 413-427.

Mörner, N.-A., 1986. Geomagnetic excursions in late Brunhes time, European long-core data. Physics of the Earth and Planetary Interiors 44, 47-52.

Mosblech, N.A., Bush, M.B., Gosling, W.D., Hodell, D., Thomas, L., van Calsteren, P., Correa-Metrio, A., Valencia, B.G., Curtis, J., van Woesik, R., 2012. North Atlantic forcing of Amazonian precipitation during the last ice age. Nature Geoscience 5, 817-820.

Müller-Karger, F., McClain, C., Fisher, T., Esaias, W., Varela, R., 1989. Pigment distribution in the Caribbean Sea: Observations from space. Progress in Oceanography 23, 23-64.

Nace, T.E., Baker, P.A., Dwyer, G.S., Silva, C.G., Rigsby, C.A., Burns, S.J., Giosan, L., Otto-Bliesner, B., Liu, Z., Zhu, J., 2014. The role of North Brazil Current transport in the paleoclimate of the Brazilian Nordeste margin and paleoceanography of the western tropical Atlantic during the late Quaternary. Palaeogeography, Palaeoclimatology, Palaeoecology 415, 3-13.

Odin, G., Fullagar, P., 1988. Chapter C4 geological significance of the glaucony facies. Developments in sedimentology 45, 295-332.

Odin, G.S., 1988. Green Marine Clays. Elsevier.

Pattier, F., Loncke, L., Gaullier, V., Basile, C., Maillard, A., Imbert, P., Roest, W.R., Vendeville, B.C., Patriat, M., Loubrieu, B., 2013. Mass-transport deposits and fluid venting in a transform margin setting, the eastern Demerara Plateau (French Guiana). Marine and Petroleum Geology 46, 287-303.

Pattier, F., Loncke, L., Imbert, P., Gaullier, V., Basile, C., Maillard, A., Roest, W.R., Patriat, M., Vendeville, B.C., 2015. Origin of an enigmatic regional Mio-Pliocene unconformity on the Demerara plateau. Marine Geology 365, 21-35.

Plenier, G., Valet, J.-P., Guérin, G., Lefèvre, J.-C., LeGoff, M., Carter-Stiglitz, B., 2007. Origin and age of the directions recorded during the Laschamp event in the Chaîne des Puys (France). Earth and Planetary Science Letters 259, 414-431.

Rama-Corredor, O., Martrat, B., Grimalt, J.O., López-Otalvaro, G.E., Flores, J.A., Sierro, F., 2015. Parallelisms between sea surface temperature changes in the western tropical Atlantic (Guiana Basin) and high latitude climate signals over the last 140 000 years. Climate of the Past 11, 1297-1311.

Rebesco, M., Camerlenghi, A., 2008. Contourites. Elseiver.

Rebesco, M., Hernández-Molina, F.J., Van Rooij, D., Wåhlin, A., 2014. Contourites and associated sediments controlled by deep-water circulation processes: State-of-the-art and future considerations. Marine Geology 352, 111-154.

Reimer, P., Bard, E., Bayliss, A., Beck, J., Blackwell, P., Bronk Ramsey, C., Buck, C., Cheng, H., Edwards, R., Friedrich, M., Grootes, P., Guilderson, T., Haflidason, H., Hajdas, I., Hatté, C., Heaton, T., Hogg, A., Hughen, K., Kaiser, K., Kromer, B., Manning, S., Niu, M., Reimer, R., Richards, D., Scott, E., Southon, J., Turney, C., van der Plicht, J., 2013. IntCal13 and MARINE13 radiocarbon age calibration curves 0-50000 years calBP Radiocarbon 55(4).

Shackleton, N.J., Sánchez-Goñi, M.F., Pailler, D., Lancelot, Y., 2003. Marine Isotope Substage 5e and the Eemian Interglacial. Global and Planetary Change 36, 151-155.

Shanmugam, G., 2016. The contourite problem. Sediment Provenance.

Smith, G., Creer, K.M., 1986. Analysis of geomagnetic secular variations 10 000 to 30 000 years bp, Lac du Bouchet, France. Physics of the Earth and Planetary Interiors 44, 1-14.

Smith, J.D., Foster, J.H., 1969. Geomagnetic reversal in Brunhes normal polarity epoch. Science 163, 565-567.

Stow, D., Faugères, J.-C., 2008a. Contourite facies and the facies model. Developments in Sedimentology 60, 223-256.

Stow, D.A.V., Faugères, J.-C., Howe, J.A., Pudsey, C.J., Viana, A.R., 2002. Bottom currents, contourites and deep-sea sediment drifts: current state-of-the-art. Bottom currents, contourites and deep-sea sediment drifts: current state-of-the-art. In: Stow, D.A.V., Pudsey, C.J., Howe, J.A., Faugères, J.-C., Viana, A.R. (Eds.), Deep-Water Contourite Systems: Modern Drifts and Ancient Series, Seismic and Sedimentary Characteristics: Geological Society London Memoir 22, 137-154.

Stow, D.A.V., Faugères, J.C., 2008b. Chapter 13 Contourite Facies and the Facies Model, In: Rebesco, M., Camerlenghi, A. (Eds.), Developments in Sedimentology. Elsevier, pp. 223-256.

Tallobre, C., 2017. Mise en évidence d'un système de dépôt contouritique et des processus sédimentaires associés sur le plateau de Demerara (marge guyanaise), Cefrem. Université de Perpignan via Domitia, Perpignan.

Tallobre, C., Loncke, L., Bassetti, M.-A., Giresse, P., Bayon, G., Buscail, R., de Madron, X.D., Bourrin, F., Vanhaesebroucke, M., Sotin, C., 2016. Description of a contourite depositional system on the Demerara Plateau: Results from geophysical data and sediment cores. Marine Geology 378, 56-73.

Thouveny, N., Williamson, D., 1988. Palaeomagnetic study of the Holocene and Upper Pleistocene sediments from Lake Barombi Mbo, Cameroun: first results. Physics of the Earth and Planetary Interiors 52, 193-206.

Tudryn, A., Tucholka, P., Gibert, E., Gasse, F., Wei, K., 2010. A late Pleistocene and Holocene mineral magnetic record from sediments of Lake Aibi, Dzungarian Basin, NW China. Journal of Paleolimnology 44, 109-121.

van der Hammen, T., Absy, M.L., 1994. Pollen and ClimateAmazonia during the last glacial. Palaeogeography, Palaeoclimatology, Palaeoecology 109, 247-261.

Viana, A.R., Faugeres, J.C., Kowsmann, R.O., Lima, J.A.M., Caddah, L.F.G., Rizzo, J.G., 1998. Hydrology, morphology and sedimentology of the Campos continental margin, offshore Brazil. Sedimentary Geology 115, 133-157.

Wiewióra, A., Giresse, P., Petit, S., Wilamowski, A., 2001. A deep-water glauconitization process on the Ivory Coast–Ghana marginal ridge (ODP site 959): determination of Fe3+-rich montmorillonite in green grains. Clays and Clay Minerals 49, 540-558.

Zaragosi, S., Bourillet, J.-F., Eynaud, F., Toucanne, S., Denhard, B., Van Toer, A., Lanfumey, V., 2006. The impact of the last European deglaciation on the deep-sea turbidite systems of the Celtic-Armorican margin (Bay of Biscay). Geo-Marine Letters 26, 317-329.

Table 1: Radiocarbon dates for well-preserved Globigerinoides sp. fractions from samples collected from core IG-KSF-11. The calibrated ages were calculated using Calib 7.0.4 with the Marine 09 calibration curve (Reimer et al., 2013).

Table 2: Tie points identified in the IG-KSF-05 and IG-KSF-11 core based on correlation with reference oxygen isotope curves (Martinson et al., 1987; Walker et al., 2009)

Table 3: Sedimentary facies table based on the description of core, microscopic observation (sand fraction and thin section).

Table 4: Average chemical composition measured by microprobe coupled to the SEM on mud and on green grains coming from the core IG-KSF-11 at different depth on the core (0 cm, 60 cm, 70 cm, 90 cm, 300 cm, 420 cm, 442 cm, 460 cm, 590 cm). For each grain, 2 measures was performed, results the average is established in function of the grain colour (yellowish-green, green, and dark green, the last one being sub-divided into dark and very dark green).

Figure 1: General map and location of the study area with position of North Atlantic Deep water (NADW) and Antarctic Bottom Water (AABW).

Figure 2: Bathymetric map with the position of cores analysed in this paper. The core IG-KSF-05 was collected inside the drift of the Demerara Contourite Depositional System (CDS) whereas the core IG-KSF-11 and IG-KSF-15 were collected inside the moat of this CDS.

Figure 3: Sedimentary log of core IG-KSF-05, collected in the sedimentary drift, presenting the identified sedimentary facies (more details about facies in table 3), the planktic (Globigerina ruber) and benthic (Uvigerina mediterranea) oxygen isotope records, the palaeomagnetism record (NRM, inclination and declination), glauconitic grain concentration on bulk sediment (total green grains with the green curve) and Ca XRF record.

Figure 4: Sedimentary log of core IG-KSF-11, collected in the contouritic moat, illustrating the identified sedimentary facies (more details about facies in table 3), planktic (Globigerina

ruber) and benthic (Uvigerina mediterranea) oxygen isotope record, the palaeomagnetism record (NRM, inclination and declination), glauconitic grain quantification on bulk sediment (total green grains with the green curve, and the bars represent the relative content in function of the greening (yellowish, green and dark green grains), the sortable silt on the free-carbonated record and Ca XRF record.

Figure 5: Sedimentary log of core IG-KSF-15, collected in the moat, with glauconitic grain quantitative estimation on bulk sediment (total green grains with the green curve) and Ca XRF record.

Figure 6: Reference isotopic curves of Guyana (López-Otálvaro et al., 2009), a global curve for the Atlantic domain (Lisiecki and Raymo, 2005; Lisiecki and Raymo, 2009; Lopes et al., 2014), North Brazil (Arz et al., 1998), and IGUANES data for cores IG-KSF-05 and IG-KSF-11.

Figure 7: Thin section photos illustrating the different micro-facies F2 to F7 (see table 3).

Figure 8: Thin section s of some sediment facies. (F: foraminifera, G.If: glauconitic infilling, Gic: glauconitic intraclast, GM: glauconitic mould, Qz: quartz)

Figure 9: Illustration of the degree of glauconitic maturity. The different degrees of maturity are illustrated by the colour of grains, the structure at the grain surface with MEB picture, the micro-structure with MEB picture, and the elementary composition measured by microprobe which is one-time the on the single related grain.

Figure 10: Schematic evolution of glauconitic grains from pristine marine mud to dark green grains with the mean elementary composition measured by microprobe and established for each class colour with the two values on each grain.

Figure 11: Schema of the ideal contouritic sequence (modified from (Stow and Faugères (2008a)) and according to the glauconitisation processes. The concentration and the mineralogic maturity of the green grains increase with the winnowing intensity.

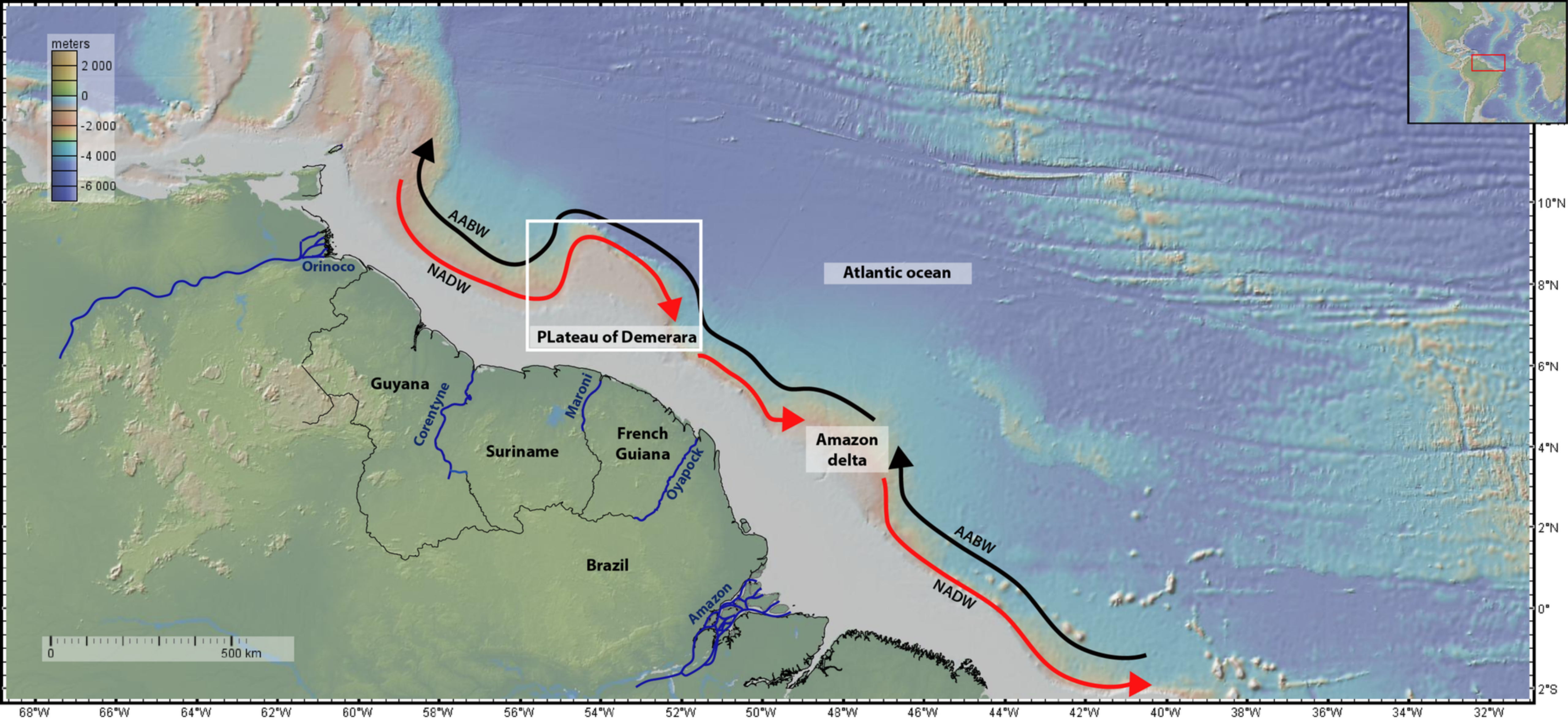

meters
2 000
0
-2 000
-4 000
-6 000
AABW
NADW
PLateau of Demerara
Atlantic ocean
Orinoco
Guyana
Corentyne
Suriname
Maroni
French Guiana
Oyapock
Amazon delta
Brazil
Amazon
AABW
NADW
0
500 km
10°N
8°N
6°N
4°N
2°N
0°
2°S
68°W
66°W
64°W
62°W
60°W
58°W
56°W
54°W
52°W
50°W
48°W
46°W
44°W
42°W
40°W
38°W
36°W
34°W
32°W

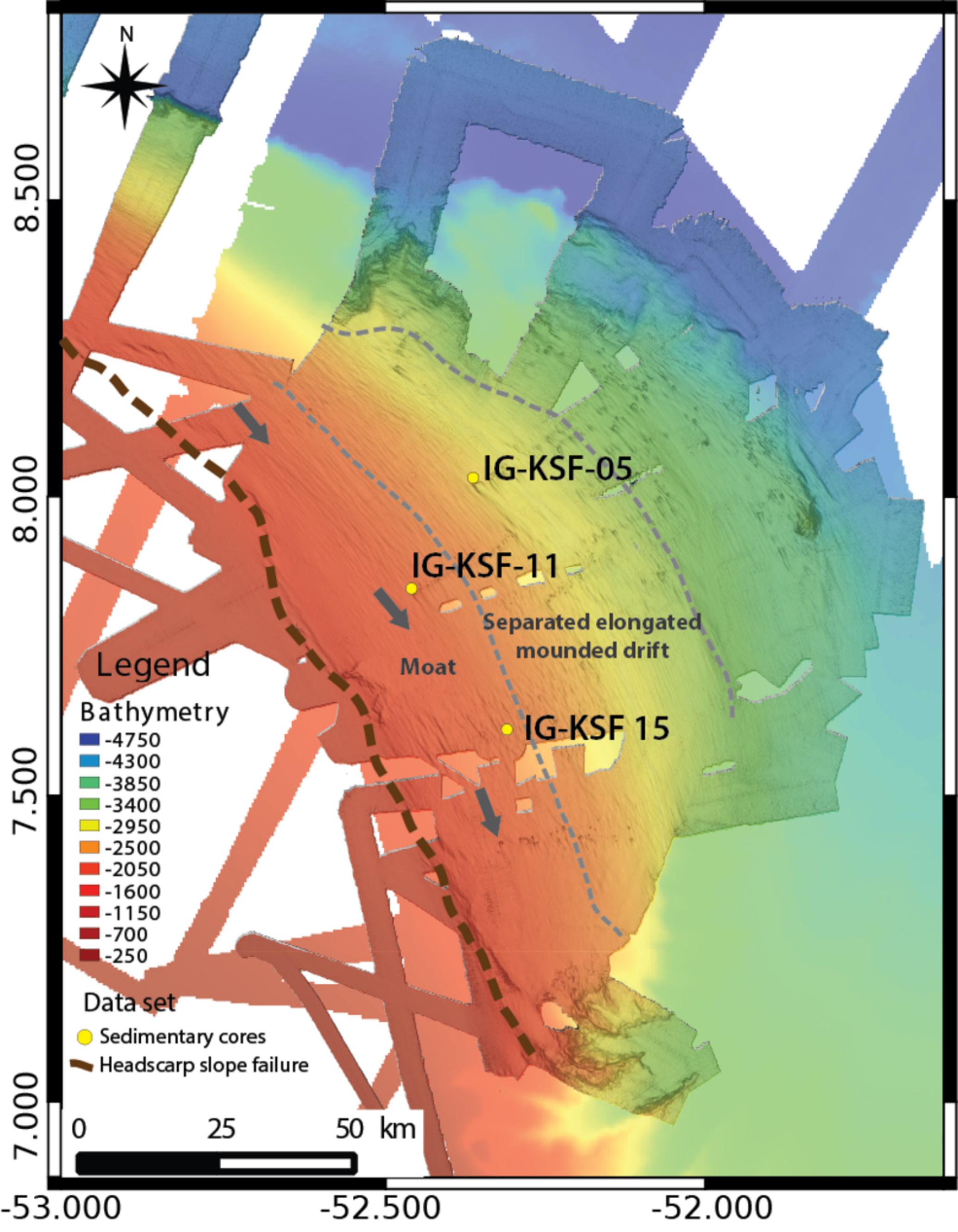
N
IG-KSF-05
IG-KSF-11
IG-KSF 15
Separated elongated
mounded drift
Moat
Legend
Bathymetry
-4750
-4300
-3850
-3400
-2950
-2500
-2050
-1600
-1150
-700
-250
Data set
Sedimentary cores
Headscarp slope failure
0
25
50 km
8.500
8.000
7.500
7.000
-53.000
-52.500
-52.000

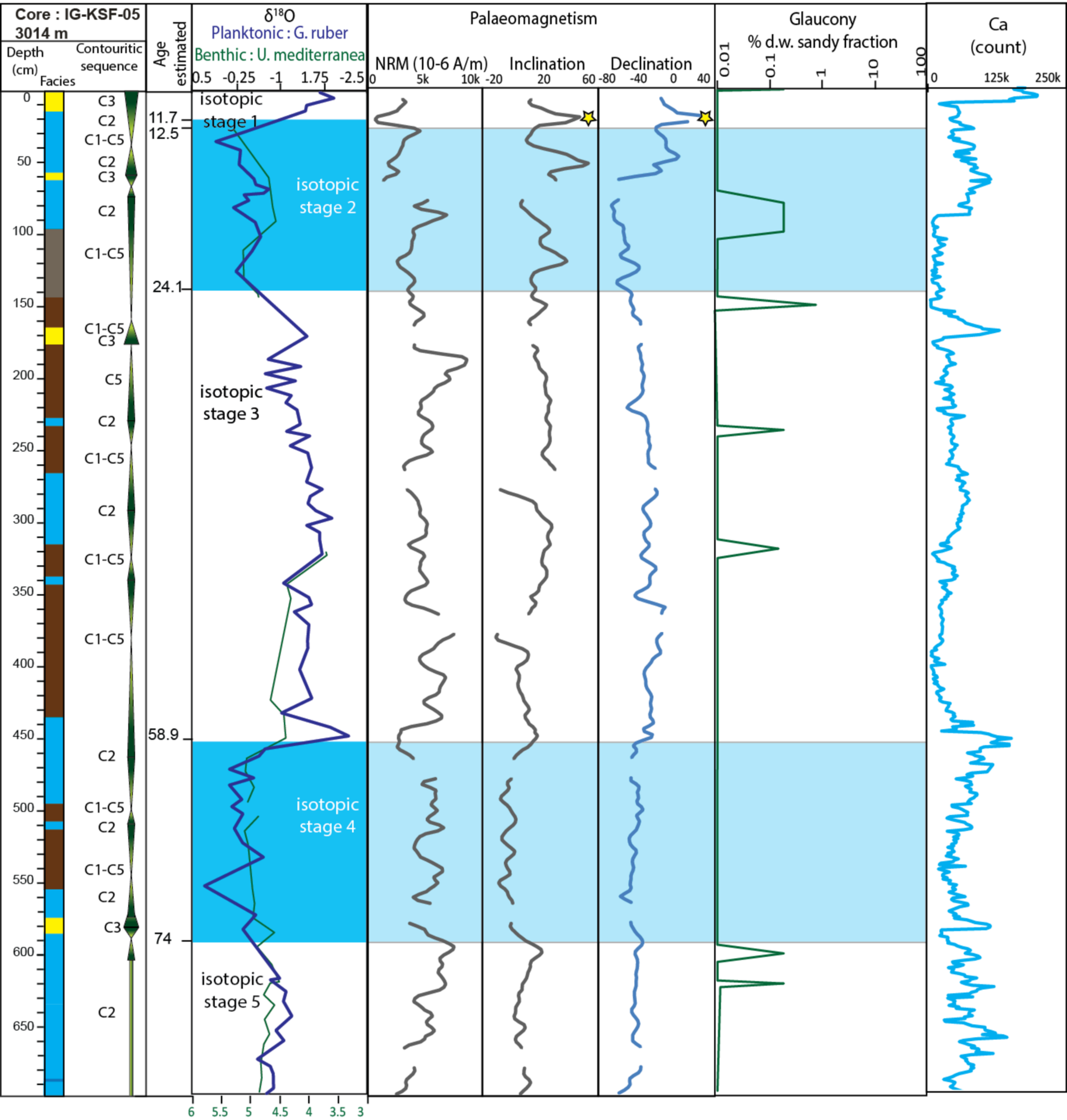

Core : IG-KSF-05
3014 m
Depth (cm)
Facies
Contouritic sequence
Age estimated
δ18O
Planktonic : G. ruber
Benthic : U. mediterranea
Palaeomagnetism
NRM (10-6 A/m)
Inclination
Declination
Glaucony
% d.w. sandy fraction
Ca (count)
isotopic stage 1
isotopic stage 2
isotopic stage 3
isotopic stage 4
isotopic stage 5
11.7
12.5
24.1
58.9
74
C1-C5
C2
C3
C5

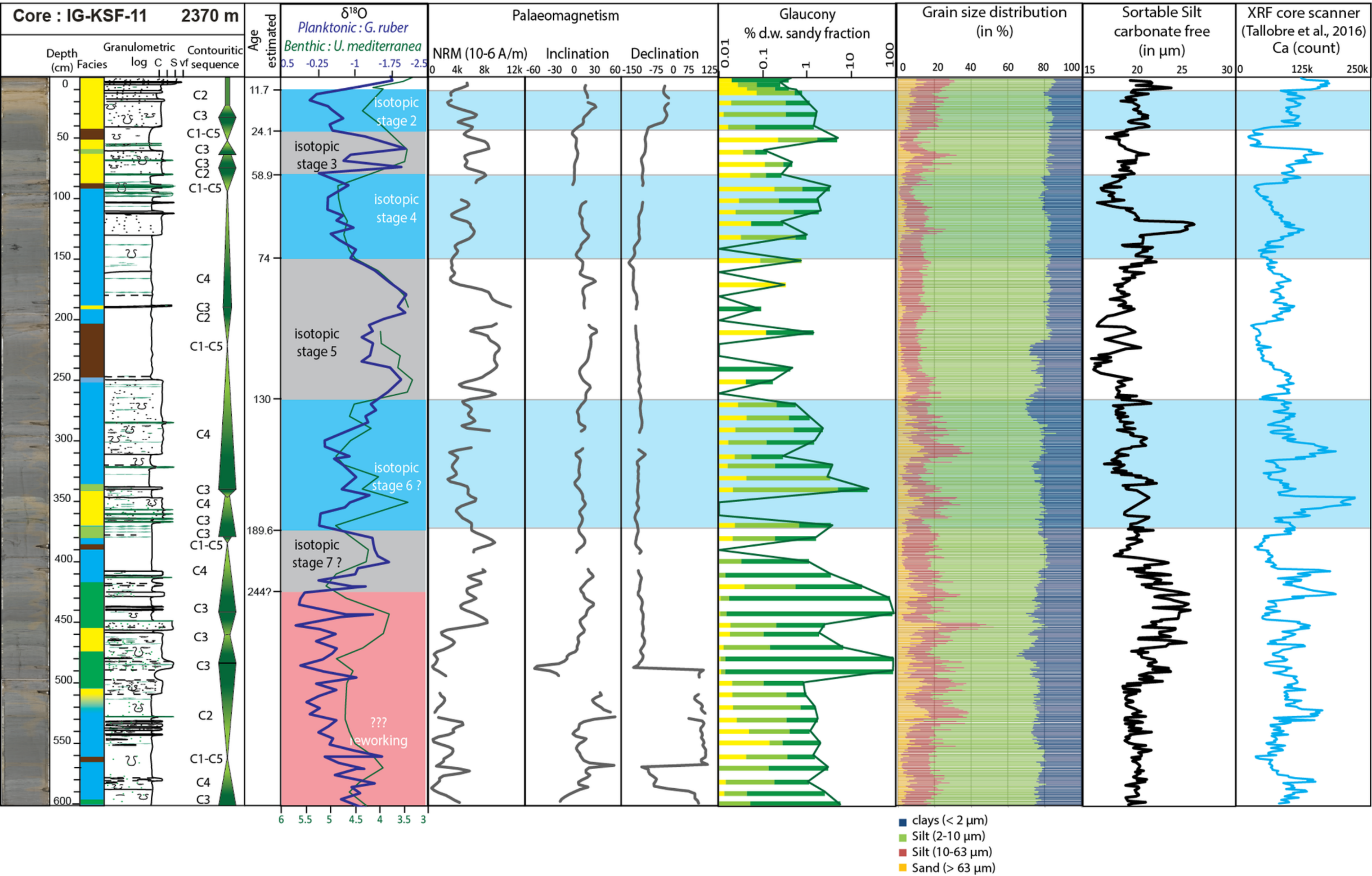

Core : IG-KSF-11 2370 m
Depth (cm)
Facies
Granulometric log
C S vf
Contouritic sequence
Age estimated
δ18O
Planktonic : G. ruber
Benthic : U. mediterranea
isotopic stage 2
isotopic stage 3
isotopic stage 4
isotopic stage 5
isotopic stage 6 ?
isotopic stage 7 ?
??? reworking
Palaeomagnetism
NRM (10-6 A/m)
Inclination
Declination
Glaucony
% d.w. sandy fraction
Grain size distribution (in %)
Sortable Silt carbonate free (in µm)
XRF core scanner (Tallobre et al., 2016) Ca (count)
clays (< 2 µm)
Silt (2-10 µm)
Silt (10-63 µm)
Sand (> 63 µm)

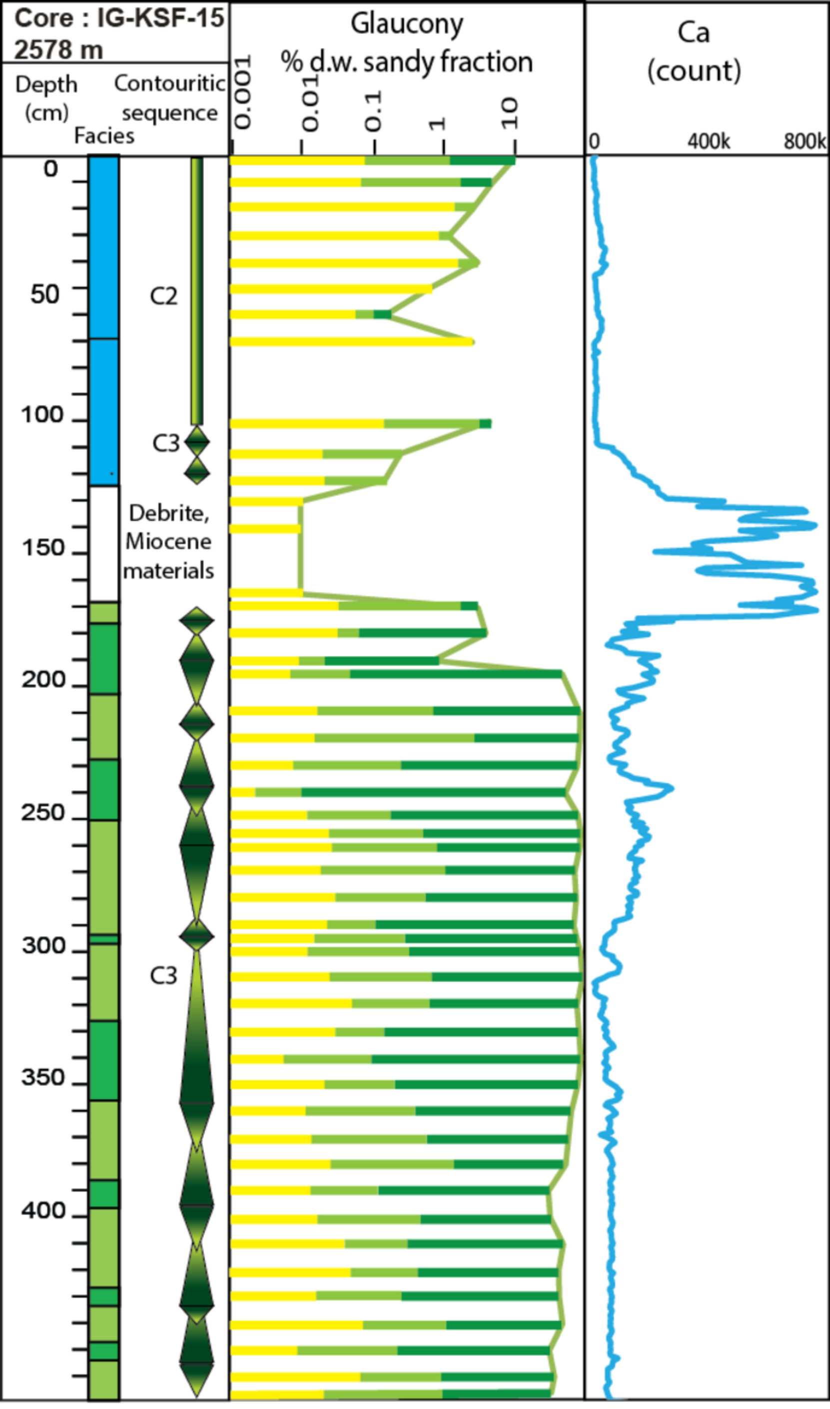

Core : IG-KSF-15
2578 m
Depth (cm)
Facies
Contouritic sequence
Glaucony
% d.w. sandy fraction
0.001
0.01
0.1
1
10
Ca
(count)
0
400k
800k
0
50
100
150
200
250
300
350
400
C2
C3
Debrite, Miocene materials
C3

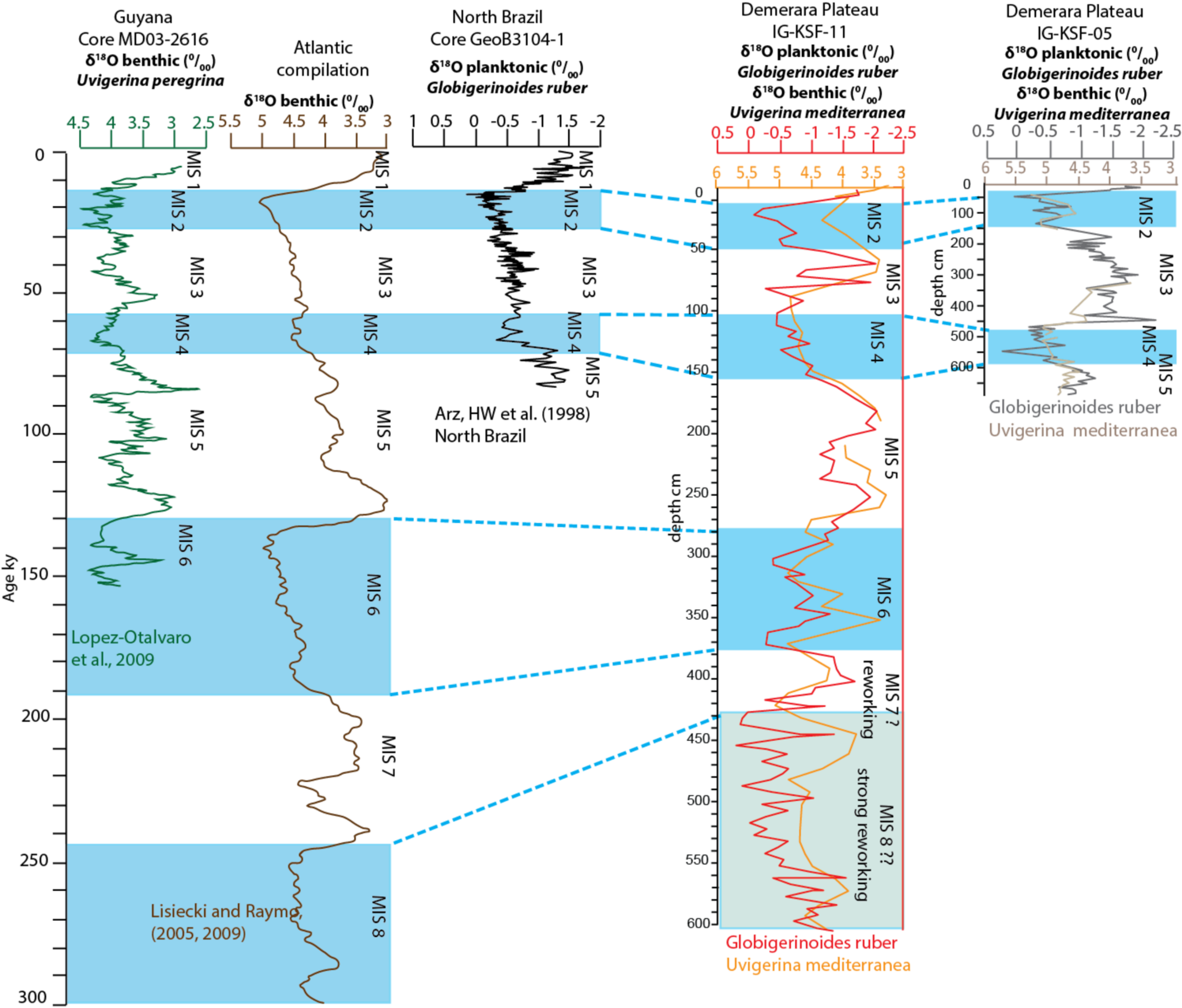

Guyana
Core MD03-2616
δ18O benthic (0/00)
Uvigerina peregrina
Atlantic compilation
δ18O benthic (0/00)
North Brazil
Core GeoB3104-1
δ18O planktonic (0/00)
Globigerinoides ruber
Demerara Plateau
IG-KSF-11
δ18O planktonic (0/00)
Globigerinoides ruber
δ18O benthic (0/00)
Uvigerina mediterranea
Demerara Plateau
IG-KSF-05
δ18O planktonic (0/00)
Globigerinoides ruber
δ18O benthic (0/00)
Uvigerina mediterranea
Age ky
depth cm
MIS 1
MIS 2
MIS 3
MIS 4
MIS 5
MIS 6
MIS 7
MIS 8
MIS 7 ?
reworking
MIS 8 ??
strong reworking
Lopez-Otalvaro et al., 2009
Lisiecki and Raymo, (2005, 2009)
Arz, HW et al. (1998) North Brazil
Globigerinoides ruber
Uvigerina mediterranea

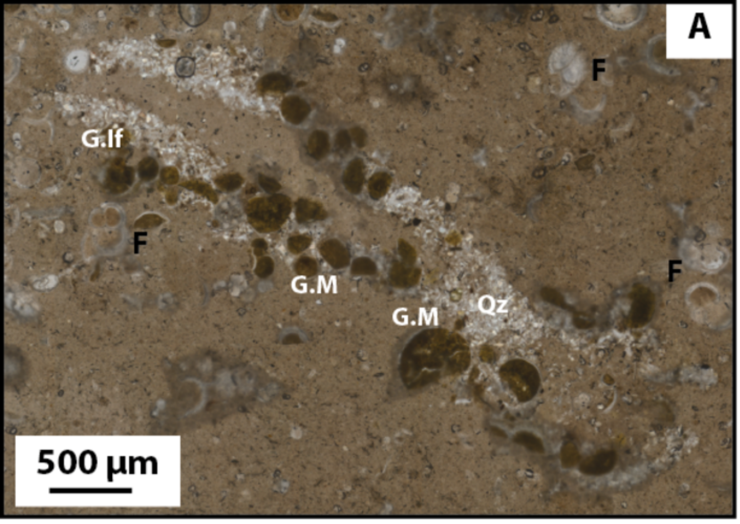

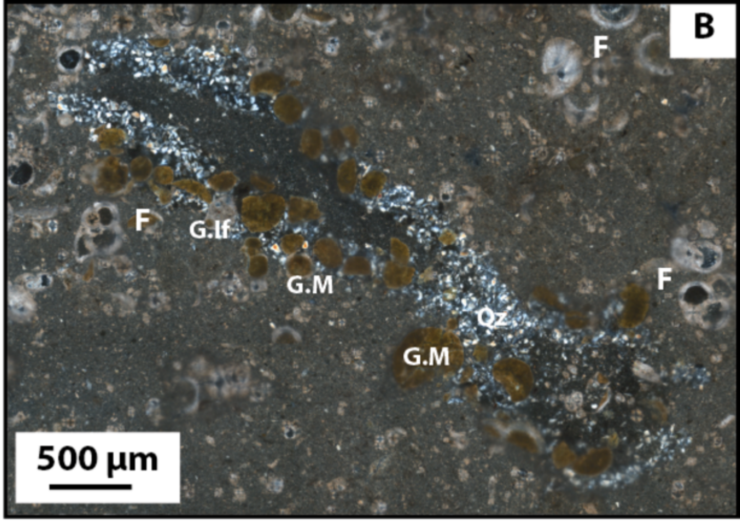

(A) in LPNA and (B) in LPA photos, illustration of bioturbation rich in glaucony and quartz in a facies F4.

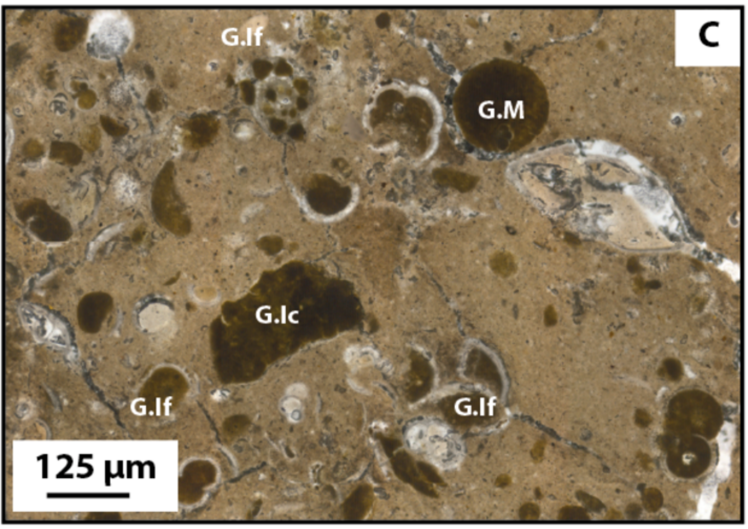

(C) LPNA photo, facies F2 with the different type of glaucony grains: inside foraminfera test, with foraminifera shape without test, and clast. Grains show a high degree of fracturing.

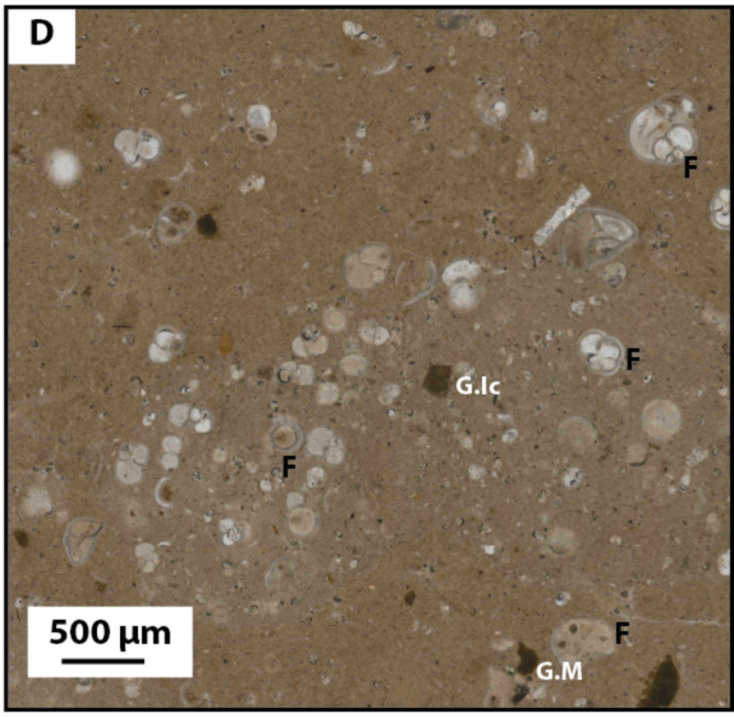

(D) LPNA photo F4, illustrated a bioturbation rich in foraminifera forming a lense in a fine mud with some grains.

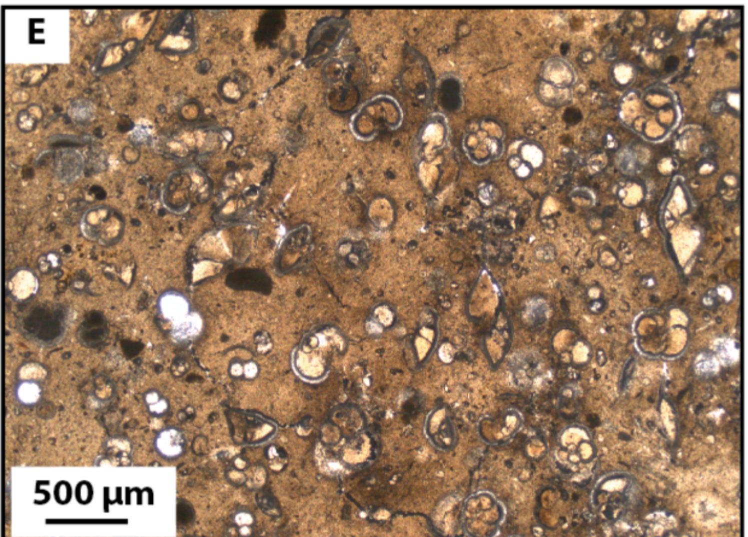

(E) LPNA photo of F3, sandy foraminifera with some glaucony grains (around 10% of glaucony), low fracturing.

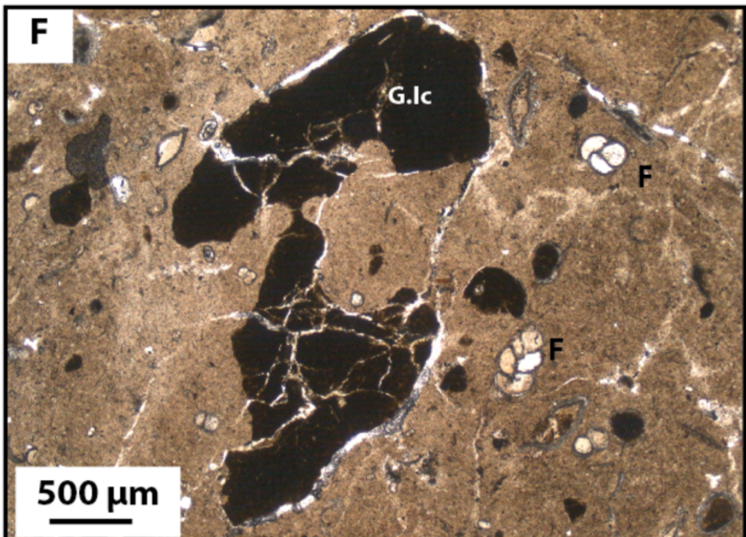

(F) LPNA photo of a glaucony clast probably coming from a glauconitic lithified surface.

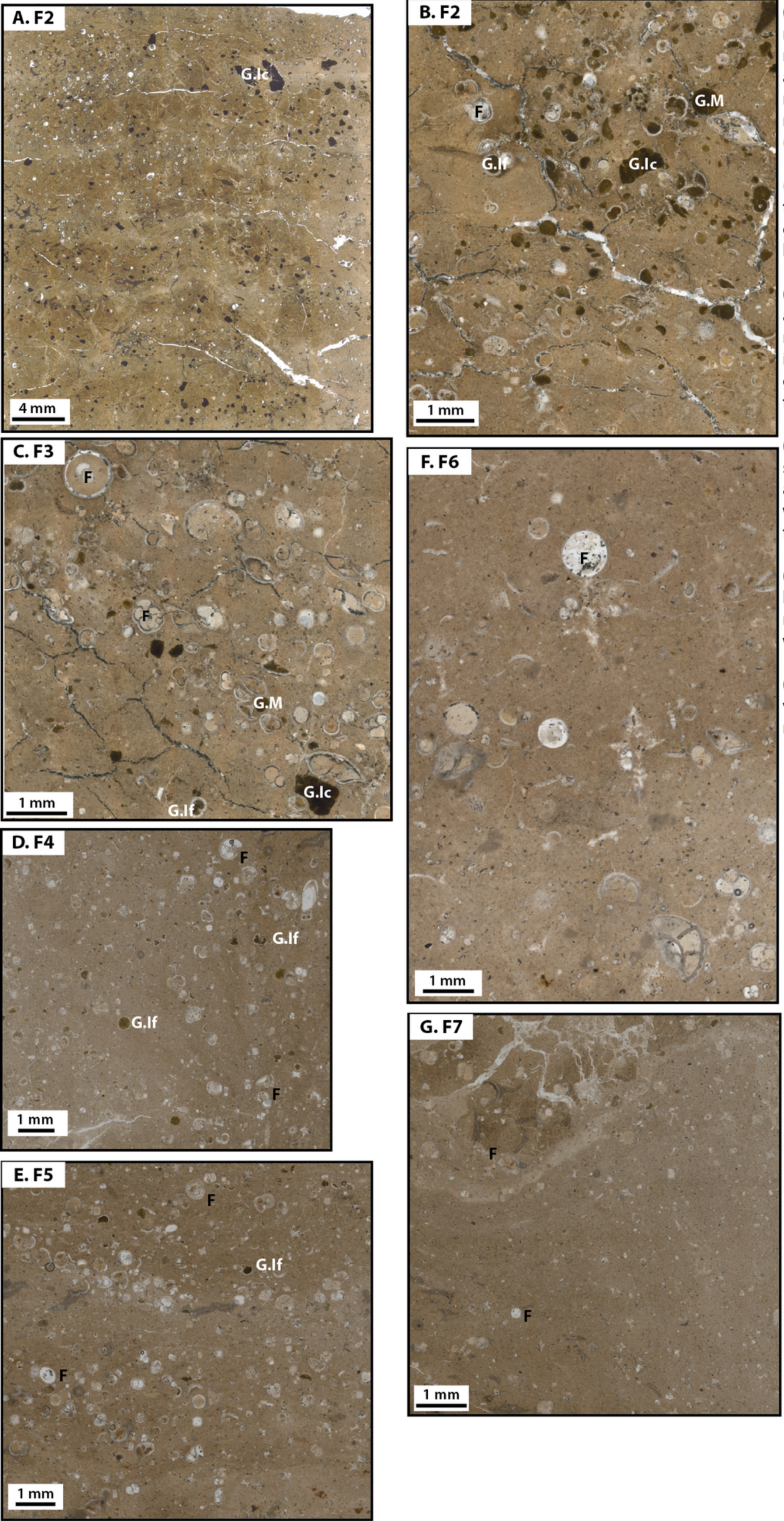

(A) and **(B)** Facies F2, glauconitic rich (*Glc*) and foraminifera rich (*F*). Glauconitic grains are present inside foraminifera test (*G.If*), foraminifera moulding (*GM*) or in intraclast (*G.Ic*).

(C) Facies F3, sandy facies foraminifera rich (*F*) and glauconitic rich (*Glc*). See laminae rich in sandy grains.

(D) Facies F4 foraminifera- and glauconitic- bearing muddy facies, moderatly rich in foraminifera (*F*) with few glauconitic grains inside foraminifera (*G If*).

(E) Facies F5, foraminifera sand rich in foraminfera (*F*) and poor in glauconitic grains with laminae rich in foraminifera.

(F) Facies F6 foraminifera bearing muddy facies, moderatly rich in foraminifera (*F*) with rare glauconitic grains.

(G) Facies F7 muddy facies , very fine facies poor in foraminifera (*F*).

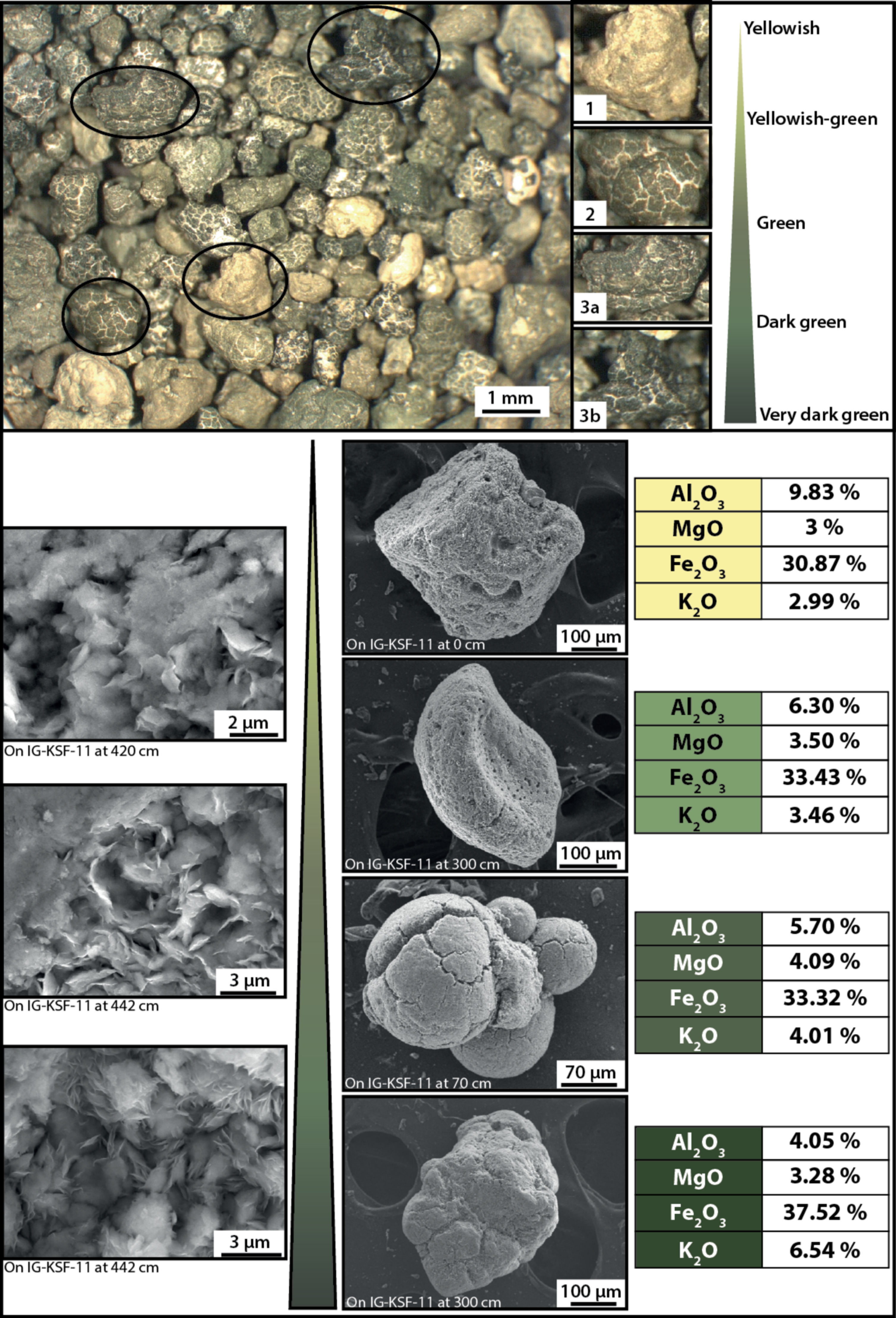

Yellowish
Yellowish-green
Green
Dark green
Very dark green
1
2
3a
3b
1 mm
2 µm
On IG-KSF-11 at 420 cm
3 µm
On IG-KSF-11 at 442 cm
3 µm
On IG-KSF-11 at 442 cm
100 µm
On IG-KSF-11 at 0 cm
Al2O3 9.83 %
MgO 3 %
Fe2O3 30.87 %
K2O 2.99 %
100 µm
On IG-KSF-11 at 300 cm
Al2O3 6.30 %
MgO 3.50 %
Fe2O3 33.43 %
K2O 3.46 %
70 µm
On IG-KSF-11 at 70 cm
Al2O3 5.70 %
MgO 4.09 %
Fe2O3 33.32 %
K2O 4.01 %
100 µm
On IG-KSF-11 at 300 cm
Al2O3 4.05 %
MgO 3.28 %
Fe2O3 37.52 %
K2O 6.54 %

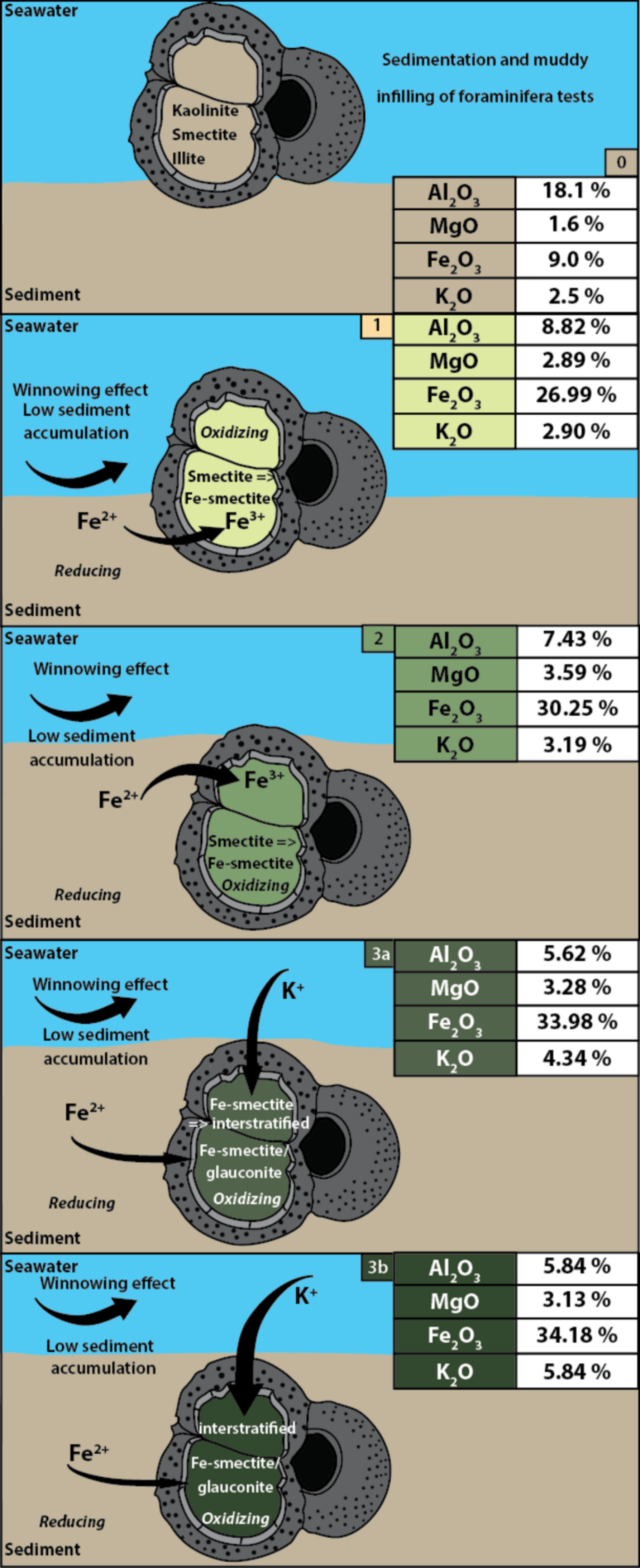
Seawater
Sedimentation and muddy infilling of foraminifera tests
Kaolinite
Smectite
Illite
0
Al2O3 18.1 %
MgO 1.6 %
Fe2O3 9.0 %
K2O 2.5 %
Sediment
Seawater
1
Al2O3 8.82 %
MgO 2.89 %
Fe2O3 26.99 %
K2O 2.90 %
Winnowing effect
Low sediment accumulation
Oxidizing
Smectite =>
Fe-smectite
Fe2+
Fe3+
Reducing
Sediment
Seawater
2
Al2O3 7.43 %
MgO 3.59 %
Fe2O3 30.25 %
K2O 3.19 %
Winnowing effect
Low sediment accumulation
Fe3+
Fe2+
Smectite =>
Fe-smectite
Oxidizing
Reducing
Sediment
Seawater
3a
Al2O3 5.62 %
MgO 3.28 %
Fe2O3 33.98 %
K2O 4.34 %
Winnowing effect
K+
Low sediment accumulation
Fe2+
Fe-smectite
=> interstratified
Fe-smectite/
glauconite
Oxidizing
Reducing
Sediment
Seawater
3b
Al2O3 5.84 %
MgO 3.13 %
Fe2O3 34.18 %
K2O 5.84 %
Winnowing effect
K+
Low sediment accumulation
interstratified
Fe2+
Fe-smectite/
glauconite
Oxidizing
Reducing
Sediment

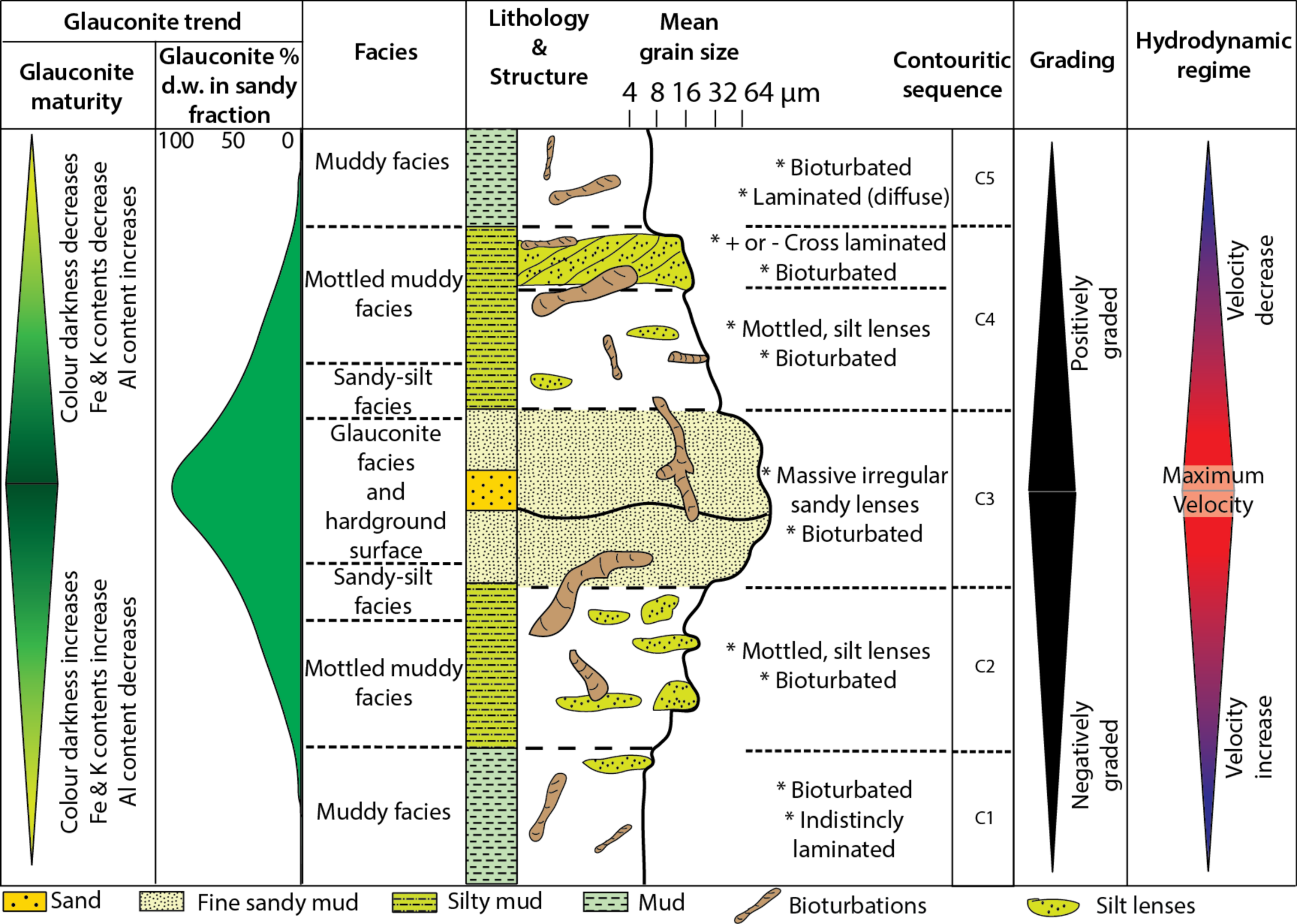
Glauconite trend
Glauconite maturity
Glauconite % d.w. in sandy fraction
100 50 0
Facies
Lithology & Structure
Mean grain size
4 8 16 32 64 µm
Contouritic sequence
Grading
Hydrodynamic regime
Colour darkness decreases
Fe & K contents decrease
Al content increases
Colour darkness increases
Fe & K contents increase
Al content decreases
Muddy facies
Mottled muddy facies
Sandy-silt facies
Glauconite facies and hardground surface
Sandy-silt facies
Mottled muddy facies
Muddy facies
* Bioturbated
* Laminated (diffuse)
* + or - Cross laminated
* Bioturbated
* Mottled, silt lenses
* Bioturbated
* Massive irregular sandy lenses
* Bioturbated
* Mottled, silt lenses
* Bioturbated
* Bioturbated
* Indistinctly laminated
C5
C4
C3
C2
C1
Positively graded
Negatively graded
Velocity decrease
Maximum Velocity
Velocity increase
Sand
Fine sandy mud
Silty mud
Mud
Bioturbations
Silt lenses

Depth core (cm)	Core	Material	Age ^{14}C (yr BP)	1 sigma calibrated age (yr cal. BP)		
				min	max	average
0	IG-KSF-11	*Globigerinoides sp.*	13 930 ± 80 BP	14 201	14 466	14 334
60	IG-KSF-11	*Globigerinoides sp.*	34 400 ± 600 BP	35 630	37 248	36 439
130	IG-KSF-11	*Globigerinoides sp.*	37 100 ± 800 BP	38 560	39 974	39 267
130	IG-KSF-11	*Globigerinoides sp.*	50 000 ± 4 000 BP			
313	IG-KSF-11	*Globigerinoides sp.*	42 700 ± 1 500 BP	42 287	45 138	43 713
452	IG-KSF-11	*Globigerinoides sp.*	48 000 ± 3 000 BP	-	-	-
530	IG-KSF-11	*Globigerinoides sp.*	49 000 ± 4 000 BP	-	-	-
530	IG-KSF-11	Mud organic matter	26 170 ± 450 BP	27 519	28 574	28 047
582	IG-KSF-11	*Globigerinoides sp.*	39 700 ± 1 100 BP	40 675	42 385	41 530
600	IG-KSF-11	*Globigerinoides sp.*	35 300 ± 700 BP	36 716	38 227	37 472
600	IG-KSF-11	*Globigerinoides sp.*	28 400 ± 200 BP	29 479	30 059	29 769
0	IG-KSF-05	*Globigerinoides sp.*	5 640 ± 40 BP	4 027	4 158	4 093
290	IG-KSF-05	*Globigerinoides sp.*	17 460 ± 100 BP	18 485	18 763	18 624
50	IG-KSF-05	*Globigerinoides sp.*	34 400 ± 600 BP	34 991	36 551	35 771
169	IG-KSF-05	*Globigerinoides sp.*	37 910 ± 870 BP	39 262	40 584	39 923
250	IG-KSF-05	*Globigerinoides sp.*	30 600 ± 400 BP	31 965	32 617	32 291
250	IG-KSF-05	Mud organic matter	24 370 ± 230 BP	26 154	26 661	26 408
340	IG-KSF-05	*Globigerinoides sp.*	44 000 ± 3000 BP	42 912	47 381	45 147
490	IG-KSF-05	*Globigerinoides sp.*	41 000 ± 2000 BP	41 339	43 001	42 170
657	IG-KSF-05	*Globigerinoides sp.*	>43 000 BP	-	-	-

table 1: Radiocarbon dates for well-preserved Globigerinoides sp. fractions from samples collected from core IG-KSF-11. The calibrated ages were calculated using Calib 7.0.4 with the Marine 09 calibration curve (Reimer et al., 2013)

IG-KSF-05

Intervals	Duration (kyr)	stade	source
0-18	0-11.7	MIS 1	Martinson et al., 1987; Walter et al., 2009
25-139	11.7-24.1	MIS 2	
139-451	24.1-58.9	MIS 3	
451-590	58.9-74	MIS 4	
?	74-130	MIS 5	

IG-KSF-11

Intervals	Duration (kyr)	stade	source
0-10	0-11.7	MIS 1	Martinson et al., 1987; Walter et al., 2009
10-43	11.7-24.1	MIS 2	
43-80	24.1-58.9	MIS 3	
80-150	58.9-74	MIS 4	
150-267	74-130	MIS 5	
267-371	130-189.6	MIS 6	
371-422 ?	189.6-244	MIS 7	
?	244-291	MIS 8	

Table 2 : Tie points identified in the IG-KSF-05 and IG-KSF-11 core based on correlation with reference oxygen isotope curves (Martinson et al., 1987; Walker et al., 2009)

	Characterisitc	Components	Glaucony maturity	Fracturation of components	Structure	Environment interpretation
F1 - Carbonate facies	Rich in carbonate, indurated mass, low hydratation of sediments	- Rare glaucony -Some iron oxyde - Foramnifera rich		Low to medium	Absence	Mass Transoprt Deposit
F2 - Glauconitic facies	Glaucony rich	- Glaucony rich - Foramnifera rich	- Dark green - Clasts	Medium to high	- Bioturbation rich - Sandy foraminifera laminae	Contourites
	Glaucony rich	- Glaucony rich - Foramnifera rich	- Dark green - Inside foramnifera or with foraminifera shape	Medium to high	- Bioturbation rich - Sandy foraminifera laminae	Contourites
F3 - Sandy facies	Foraminifera rich, glauony in foraminifera	- Glaucony rich - Foramnifera rich - Quartz in biotrubation	- Light to dark green - Inside foramnifera or with foraminifera shape	Medium to high	- Bioturbation rich - Sandy foraminifera laminae	Contourites
F4 - Foraminifera- and glauconitic-bearing Muddy facies	Glaucony and foraminifera rich	- Some glaucony - Foramnifera rich -Some iron oxyde - Quartz in biotrubation	- Glaucony in foraminifera test or with foraminifera shape - Light to medium green	Low to medium	Bioturbation rich	Contourites
F5 - Foraminifera sand	Foraminifera rich without glaucony	- Rare foramnifera	- Low glaucony and sometimes none glaucony	Low	Bioturbation rich	Hemipelagite
F6 - Foraminifera bearing Muddy facies	Foraminifera rich with little glaucony	- Rare glaucony - Foramnifera rare -Some iron oxyde	- Low glaucony and sometimes none glaucony	Low	- Bioturbation rich - Sandy foraminifera lenses	Hemipelagite
F7 - Muddy facies	Very fine matrix and grains poor	- Rare glaucony - Foramnifera rare -Some iron oxyde	- Low glaucony and sometimes none glaucony	Low	Low to high Bioturbation	Hemipelagite

	Al_2O_3	MgO	Fe_2O_3	K_2O	SiO_2
Mud	18.1%	1.6%	9.0%	2.5%	46.8%
Greenish/ yellowish grain	8.8%	2.9%	27.0%	2.9%	47.1%
Green grain	7.4%	3.6%	30.3%	3.2%	51.2%
Dark green grain	5.6%	3.3%	34.0%	4.3%	49.1%
Very dark green grain	5.8%	3.1%	34.2%	5.4%	48.6%

Table 4 : Average chemical composition measured by microprobe coupled to the SEM on mud and on green grains coming from the core IG-KSF-11 at different depth on the core (0 cm, 60 cm, 70 cm, 90 cm, 300 cm, 420 cm, 442 cm, 460 cm, 590 cm).